Mesoscale, tidal and seasonal/interannual drivers of the Weddell Sea overturning circulation

Andrew L. Stewart*

Department of Atmospheric and Oceanic Sciences, University of California, Los Angeles, California, USA

ABSTRACT

The Weddell Sea supplies 40–50% of the Antarctic Bottom Waters that fill the global ocean abyss, and therefore exerts significant influence over global circulation and climate. Previous studies have identified a range of different processes that may contribute to dense shelf water (DSW) formation and export on the southern Weddell Sea continental shelf. However, the relative importance of these processes has not been quantified, which hampers prioritization of observational deployments and development of model parameterizations in this region. In this study a high-resolution (1/12°) regional model of the southern Weddell Sea is used to quantify the overturning circulation and decompose it into contributions due to multi-annual mean flows, seasonal/interannual variability, tides, and other sub-monthly variability. It is shown that tides primarily influence the overturning by changing the melt rate of the Filchner-Ronne Ice Shelf (FRIS). The resulting ∼0.2 Sv decrease in DSW transport is comparable to the magnitude of the overturning in the FRIS cavity, but small compared to DSW export across the continental shelf break. Seasonal/interannual fluctuations modestly influence the overturning circulation, due to the relatively short (8-year) analysis period. Analysis of the energy budget indicates that the non-tidal, sub-monthly variability is primarily baroclinically-generated eddies associated with dense overflows. These eddies play a comparable role to the mean flow in exporting dense shelf waters across the continental shelf break, and account for 100% of the heat transfer onto the continental shelf. The eddy component of the overturning is sensitive to model resolution, decreasing by a factor of ∼2 as the horizontal grid spacing is refined from 1/3° to 1/12°.

1. Introduction

Antarctic Bottom Water (AABW) fills approximately 36% of the global deep ocean (Johnson 2008), and its circulation comprises the deepest limb of the global overturning circulation (Orsi et al. 1999; Talley 2013). This circulation supplies oxygen to the abyssal ocean (Orsi et al. 2001), and serves as a reservoir of carbon dioxide that may mediate millennial-timescale climate evolution (Adkins 2013). AABW is primarily sourced from a few formation sites around the Antarctic continental shelf (Jacobs 2004; Ohshima et al. 2013). Of these sites, the southern Weddell Sea accounts for approximately 8 Sv ($1\,\mathrm{Sv} = 10^6\,\mathrm{m}^3/\mathrm{s}$) of the 10–20 Sv total AABW production (Jullion et al. 2014; Vernet et al. 2019). This implies that processes occurring on the southern Weddell Sea continental shelf exert substantial influence over global deep circulation, and thus potentially also over global climate.

The variety of AABW that is exported from the Weddell Sea is referred to as Weddell Sea Deep Water (WSDW) (Carmack and Foster 1975; Foster and Carmack 1976). WSDW formation results from a series of water mass transport and transformation processes over the southern Weddell Sea continental shelf and slope and in the ice shelf cavities (Foldvik and Gammelsrød 1988), which are reviewed in detail by Nicholls et al. (2009). Briefly, the southern Weddell Sea continental shelf (see *e.g.* Fig, 1(a)) hosts several, relatively light water masses: Winter Waters (WW) produced by winter cooling of local surface waters (Foster and Carmack 1976), Eastern Slope Waters (ESW) advected westward by the Antarctic Slope Current (ASC) (Fahrbach et al. 1994; Graham et al. 2013), and intrusions of modified Warm Deep Water (mWDW) from mid-depth offshore (*e.g.* Nicholls et al. 2008; Darelius et al. 2016). These lighter shelf water masses are then transformed into dense High Salinity Shelf Water (HSSW) via brine rejection during winter sea ice formation, particularly around Berkner island (Nicholls et al. 2001) and along the western front of the Ronne ice shelf (Nicholls et al. 2003; Haid and Timmermann 2013). Part of the HSSW is steered by water column thickness variations the bathymetry and ice shelf draft) through the Filchner-Ronne Ice Shelf (FRIS) cavity (Grosfeld and Gerdes 1998; Nicholls et al. 2009). During this transit the HSSW melts the base of the ice shelf (see *e.g.* Dinniman et al. 2016), which leads to its further transformation into Ice Shelf Water (ISW), characterized by potential temperatures below the surface freezing temperature (Foldvik et al. 2004; Darelius et al. 2014). The ISW exits the FRIS cavity via the Filchner trough (Darelius and Sallee 2018), and overflows onto the continental slope through the mouth of the Filchner Trough (Darelius et al. 2009; Daae et al. 2018). Finally, the overflowing waters entrain overlying mWDW as they descend and travel westward along the continental slope, completing their transfor-

**Corresponding author*: Andrew L. Stewart, astewart@atmos.ucla.edu

mation into WSDW (Carmack and Foster 1975; Muench and Gordon 1995).

In this study our focus is on the processes that control the various water mass transport and transformation processes that produce WSDW. Previous studies have identified various forms of variability in the Weddell Sea, and at other dense water formation sites, that contribute to dense water formation and export around Antarctica (Thompson et al. 2018). For example, the pronounced seasonal cycle in the atmospheric conditions over the southern Weddell Sea dictates the timing of HSSW production in front of the Ronne ice shelf front (Nicholls et al. 2008), and thus influences the export of ISW across the Filchner ice shelf front, and the overflow of ISW at the mouth of the Filchner Trough (Wang et al. 2012; Daae et al. 2018). Tidal flows increase the rate at which the FRIS, and other ice shelves, melt by increasing the amplitude of the flow variability adjacent to the ice-ocean boundary layer (Mueller et al. 2018; Hausmann et al. 2020), and enhance mixing in the boundary layer over the continental slope (Fer et al. 2016) and at the ice shelf base (Makinson and Nicholls 1999). Tides also produce rectified mean transports, particularly in the Weddell Sea, where the tidal amplitude is relatively large (Robertson 2001). These rectified transports have been implicated to increase rates of cross-shelf water mass exchange in the Ross Sea (Padman et al. 2009; Wang et al. 2013). Finally, water mass transports may be modulated by mesoscale variability, such as the formation of topographic vorticity waves (Marques et al. 2014; Daae et al. 2019) and mesoscale eddies (Baines and Condie 1998; Wang et al. 2009; Thompson et al. 2014) by vortex stretching and/or baroclinic instability in dense water overflows. Mesoscale variability excited by overflows has been shown to produce vertical transfers of momentum that drive local onshore transport of mWDW (Stewart and Thompson 2016; Morrison et al. 2020).

Although various mechanisms have been shown to play a role in the Weddell Sea overturning circulation, a quantitative evaluation of their respective contributions to the various water mass transports and transformations remains lacking. This hampers both observational deployments in the region, which typically prioritize salient processes in their planning, and the development of parameterizations for climate models, which must prioritize the most climatically impactful processes. In this study we use a regional model of the Weddell Sea to diagnose these transports and transformations, and to partition them between multi-annual mean flow, seasonal/interannual variability, mesoscale variability, and tidal flows. In Section 2 we describe the regional model configuration, describe salient aspects of the simulated circulation, and compare the simulated export of dense shelf water with observations. In Section 3 we quantify the overturning circulation in the Weddell Sea using techniques that either emphasize water mass transports or transformations, and quantify the temporal variability in the overturning. In Section 4 we decompose the Weddell Sea water mass transports/transformations and heat/salt fluxes into contributions from the multi-annual mean flow, seasonal/interannual variability, tidal flows, and other sub-monthly ("eddy") variability, and compare salient aspects of the simulated circulation across different model horizontal resolutions. Finally, in Section 5 we summarize our key findings and conclude.

2. The Weddell Sea Regional Model

We use the regional model configuration developed by Hazel and Stewart (2020) for all analysis in this study. Here we describe salient aspects of the model configuration to provide context, and evaluate the model's simulation of dense shelf water outflows against observations.

a. Model configuration

Our regional model simulates the ocean and sea ice state in southern Weddell Sea, defined for the purposes of this study to lie south of 64°S and west of 21°E. The full model domain is shown in Fig. 1(a). The base model framework is the MIT general circulation model (MITgcm, Marshall et al. 1997a,b), which we use to solve the Boussinesq hydrostatic primitive equations in geopotential coordinates, with the equation of state given by Jackett and Mcdougall (1995). We parameterize the effects of subgridscale turbulence via the K-Profile Parameterization (Large et al. 1994), in addition to a biharmonic viscosity that scales with the local horizontal grid spacing Δ_h and time step Δ_t as $A_4 = 0.003125\Delta_h^4/\Delta_t$, and a quadratic sea floor/ice shelf drag coefficient of $C_\mathrm{d} = 2.1 \times 10^{-3}$. Note that we do not utilize any parameterization of mesoscale eddy transport or isopycnal mixing, in order to allow comparison of the effects of the simulated eddies across different model resolutions. The sea ice evolves according to standard formulations for the conservation of mass and momentum (Losch et al. 2010), with internal stresses parameterized via a viscous-plastic rheology (Hibler III 1979; Zhang and Hibler III 1997). Static ice shelves and ice shelf cavities are included in the model (Losch 2008), with both the sea floor bathymetry and the ice shelf draft derived from the RTopo-2 product (Schaffer et al. 2014), as shown in in Fig. 1.

The model is forced via the open boundaries at its northern and eastern edges, and via its interaction with a prescribed atmospheric state. At the open boundaries we prescribe the ocean and sea ice state, derived from the Southern Ocean State Estimate (SOSE) (Mazloff et al. 2010). We selected SOSE because it allows relatively high horizontal resolution of the inflowing ASC, but its short duration necessitated the use of monthly climatological boundary conditions, rather than a complete 2007–2015 boundary state (see Hazel and Stewart (2020)). Fig. 1(a)

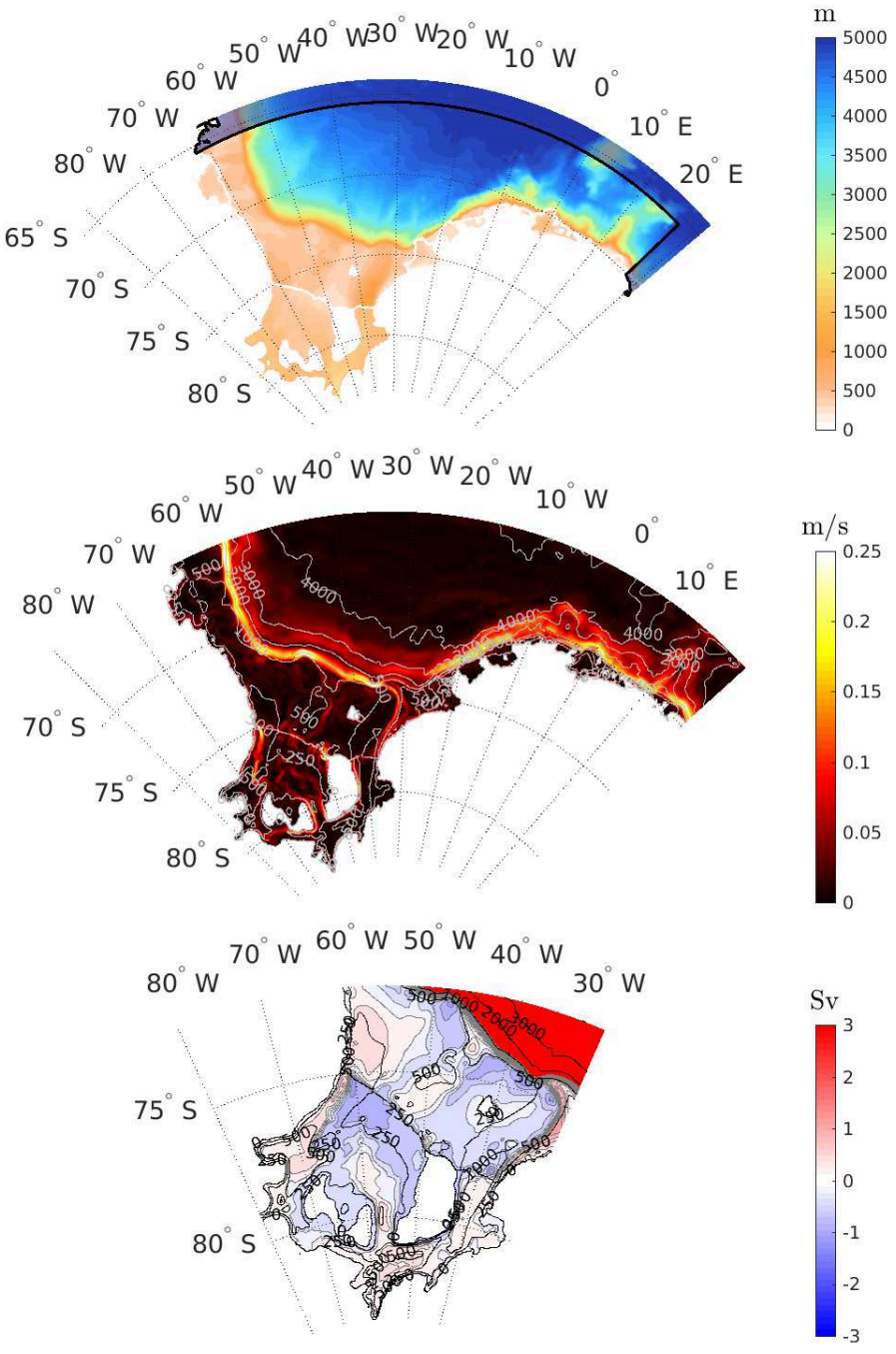

FIG. 1. Overview of the Weddell Sea Regional Model configuration. (a) Model bathymetric depth in meters. The dark gray shading indicates the region in which open boundary restoring is applied. We omit this region from subsequent plots. (b) Speed of the depth-averaged, time-mean flow. Contours indicate water column thickness in meters. (c) Barotropic streamfunction computed from the time-mean flow on the southern Weddell Sea continental shelf and within the FRIS cavity. The depth-integrated flow circulates clockwise around red regions and counter-clockwise around blue regions. The gray contour interval is 0.25 Sv, and black contours indicate water column thickness in meters. In panels (b) and (c) the time average is taken over the full 8-year analysis period in our TIDES12 simulation (see Section 2).

shows the near-boundary region in which we apply restoring in order to ensure a smooth transition between the open boundary conditions and the interior of the model domain. We exclude these regions from subsequent anal-

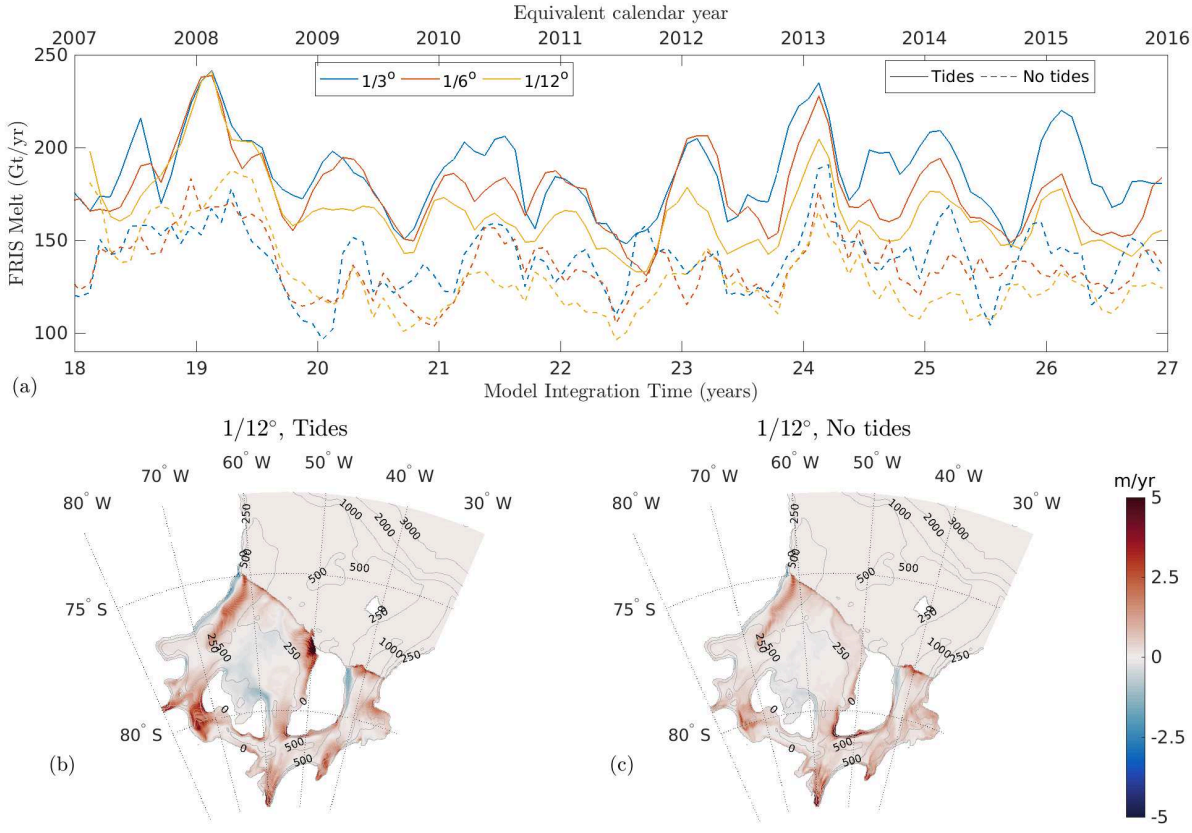

FIG. 2. Illustration of our different model experiments and spin-up procedure via the melt rate of the Filchner–Ronne Ice Shelf (FRIS). (a) Area-integrated FRIS melt rate in our six simulations at different horizontal grid spacings, and with or without tidal forcing at the model's open boundaries. (b,c) Local melt rates averaged over the full 9-year period shown in panel (a), in (a) our TIDES12 and (b) our NOTIDES12 simulation. Note that data from the first month of the 1/12° simulations is missing because successive adjustments of the model time step were necessary to stabilize these simulations over their first month of integration.

ysis due to the strong influence of the artificial restoring. We also use the open boundaries to force the tides: we impose fluctuations of the horizontal velocity fields derived from the CATS2008b solution (Padman et al. 2002) for ten tidal components (M_2, S_2, N_2, K_2, K_1, O_1, P_1, Q_1, M_f , and M_m). Atmosphere-sea ice and atmosphere-ocean exchanges are computed via standard bulk formulae, using a daily-averaged atmospheric state from the Antarctic Mesoscale Prediction System (AMPS, Powers et al. 2012). This approach avoids the need to couple the ocean and sea ice to a prognostic atmospheric model, but carries the caveat that variability in the ocean/sea ice may be artificially suppressed by the absence of coupled interactions with the atmosphere. The model forcing period spans 2007–2015, *i.e.* a total of 9 years.

For the purposes of this study we ran six simulations: we varied the model's horizontal grid spacing across 1/3°, 1/6° and 1/12°, and we ran simulations at each horizontal resolution with and without the inclusion of tidal forcing. We refer to these simulations via the abbreviations TIDES3, TIDES6 and TIDES12, corresponding to the 1/3°, 1/6° and 1/12° resolution runs with tidal forcing, and NOTIDES3, NOTIDES6 and NOTIDES12, corresponding to the 1/3°, 1/6° and 1/12° resolution runs with no tidal forcing. This suite of experiments allows us to compare representations of the Weddell Sea overturning circulation with and without influence of tides, and with increasingly fine resolution of mesoscale processes. At the highest resolution (1/12°), the grid spacing is approximately 2 km at the front of the FRIS. Thus this simulation may be expected to permit mesoscale eddies, but may not fully resolve them (Stewart and Thompson 2015a). Note that all other model parameters were held constant across this suite of simulations, with the exception of the time step, in order to allow for a controlled comparison between simulations.

We integrated our simulations forward in time at successively higher resolutions: the 1/3° runs were initialized from the reference simulation reported by Hazel and Stewart (2020) and integrated over one 9-year AMPS forcing cycle. The 1/6° runs were then initialized from the state

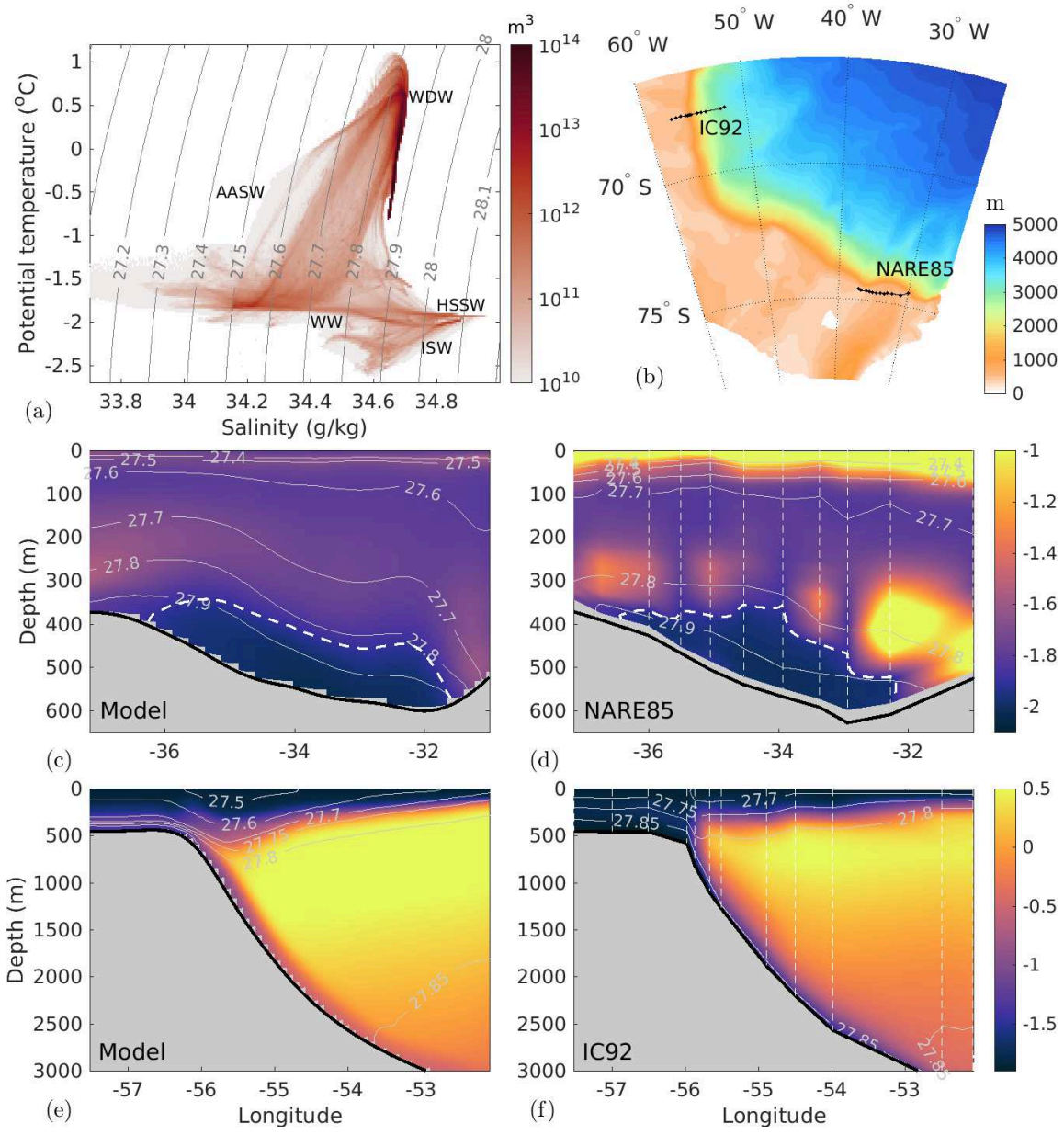

FIG. 3. Simulated water masses in our TIDES12 simulation, and comparison with observations of dense shelf water (DSW) outflows in the region. (a) Volumetric temperature/salinity diagram, showing total model volume in each $0.025\,\mathrm{g\,kg^{-1}} \times 0.005°\mathrm{C}$ area in θ–S space. The volumes are calculated using θ and S averaged over the full 8-year analysis period. The properties of various previously-identified water masses are indicated approximately (Nicholls et al. 2009): Antarctic Surface Water (AASW), Warm Deep Water (WDW), Winter Water (WW), High Salinity Shelf Water (HSSW) and Ice Shelf Water (ISW). (b) Locations of cast measurements from the NARE85 (Østerhus 2006) and IC92 (Huber 2010) cruises that are used for comparison with the modeled water masses. (c,d) Potential temperature (colors) and potential density (contours) across the NARE85 section from (c) the model state and (d) the NARE85 measurements. the white dashed line shows the $-1.9°$C isotherm, which is the approximate upper boundary of ISW. (e,f) Potential temperature (colors) and potential density (contours) across the IC92 section from (e) the model state and (f) the IC92 measurements. Panel (a) uses time-averaged hydrography over the 8-year analysis period. Panel (c) shows averages over all austral summer months (December, January and February) within the 8-year analysis period, and panel (e) shows averages over all austral winter months (June, July and August) within the 8-year analysis period. All simulation output is drawn from the TIDES12 simulation. In panels (c–f) the black curves indicate the depths of the model's bathymetry product or the measured sea floor depth.

of the 1/3° runs at the end of year 9, and both sets of runs were continued for a further 9-year forcing cycle. Finally, the 1/12° runs were similarly initialized from the state of the 1/6° runs after 18 years, and then all six runs were integrated over a final 9-year forcing cycle. We define an analysis period spanning years 20 through 27, equivalent to calendar years 2008 through 2015, to allow a year for the 1/12° runs to spin up. To illustrate this spin-up procedure and evaluate the equilibration of the simulations, in Fig. 2(a) we plot the area-integrated FRIS melt rate. All of the simulations show no statistically significant trend in the simulated FRIS melt rate[1], nor in the FRIS cavity-averaged salinity and potential temperature (not shown), between $t = 19$ yr and $t = 27$ yr. The time-mean melt rates range from 127 Gt/yr to 186 Gt/yr (see Section 4), all of which lie within the observation uncertainty of 58–190 Gt/yr reported by Moholdt et al. (2014).

b. Circulation and water masses

Hazel and Stewart (2020) provide an extensive evaluation of the model against available observations of the regional hydrography, sea ice cover and sea surface elevation, albeit in a low-resolution (1/3°) configuration. We therefore now provide an overview of the simulated regional circulation at high resolution (1/12°) and compare it with previous studies. Additional model validation and exposition of the lower-resolution simulations are provided in the Supplementary Material.

Fig. 1(b) shows the speed of the depth-averaged time-mean flow in the TIDES12 simulation. The most prominent feature of this circulation is the ASC (Thompson et al. 2018), which circulates around the edge of the Weddell Gyre. The ASC forms a relatively narrow current system upstream of the Weddell Sea (Naveira Garabato et al. 2002; Chavanne et al. 2010), but broadens as the continental slope widens in the southern and western Weddell Sea, supporting multiple frontal currents (Thompson and Heywood 2008). Various narrow currents are also visible in the FRIS cavity; to more clearly visualize these specific flows, in Fig. 1(c) we plot the barotropic streamfunction in the FRIS cavity. The barotropic streamlines pass southward across the front of the Ronne ice shelf, then southeastward through the Filchner cavity, and finally northward across the front of the Filchner ice shelf and toward the continental shelf break. This circulation is consistent with the pathway of HSSW inferred from previous observations and regional modeling studies (Grosfeld and Gerdes 1998; Nicholls et al. 2009), and the magnitude of the throughflow (~0.6 Sv) is almost identical to that reported by Hausmann et al. (2020).

The circulation beneath the FRIS is closely related to its rate of basal melt, which depends on both the temperature and the flow speed ajdacent to the ice-ocean boundary layer (Jourdain et al. 2017; Malyarenko et al. 2020). In Figs. 2(b–c) we plot the spatial distributions of the FRIS basal melt rate in our TIDES12 and NOTIDES12 simulations. The patterns of melt and freezing are qualitatively and quantitatively similar to those reported in previous observational and modeling studies (Moholdt et al. 2014; Schodlok et al. 2016; Naughten et al. 2019; Hausmann et al. 2020). The most rapid melting occurs close to the grounding lines along the southern edge of the FRIS cavity, and along the fronts of the Filchner and Ronne ice shelves, while freezing occurs primarily in the central Ronne ice shelf. The inclusion of tides primarily increases melting near the front of the Ronne ice shelf and near the southwestern grounding lines. This conforms to the findings of Hausmann et al. (2020), but differs from the findings of Mueller et al. (2018), who found that tides only served to increase melt rates near the grounding lines. The time-averaged net FRIS mass loss of 163 Gt/yr in the TIDES12 simulation is very close to the 159 Gt/yr derived from a model with similar horizontal resolution by Hausmann et al. (2020). However, we find a higher time-mean FRIS mass loss of 127 Gt/yr in the absence of tides, whereas Hausmann et al. (2020) found that removing tides reduced the FRIS mass loss to 105 Gt/yr.

The most relevant features of the southern Weddell Sea continental shelf for this study are the water mass properties and the pathways of dense shelf water (DSW), which we use to refer to both HSSW and ISW. Fig. 3(a) shows the distribution of water masses in the entire model domain via a volumetric potential temperature/salinity diagram. The water masses that participate in the overturning circulation, discussed in Section 1, generally compare well with previous *in situ* measurements, *e.g.* as summarized by (Nicholls et al. 2009). To evaluate the representation of DSW specifically, in Figs. 3(b–f) we compare the simulated export across the mouth of the Filchner Trough (panels c and d) and along the continental slope in the southwestern Weddell Sea (panels e and f). Fig. 3(b) shows the locations of the observations (Østerhus 2006; Huber 2010). We assume the observations to be representative of the seasons in which the measurements were made, and so compare them with the model output averaged over the corresponding seasons, *i.e.* over December-January-February for NARE85 and over June-July-August for IC92.

While we should not expect close quantitative agreement because we are comparing seasonally-averaged output from the model with observational snapshots, the simulated and observed DSW layers compare favorably in both sections. At the NARE85 section (Figs. 3(c–d)) the ISW layer occupies a similar portion of the Filchner Trough in the model as it does in the observations. However, the intrusions of mWDW at mid-depth are warmer by ~0.5°C

[1]The linear trend in the difference between melt rates at different resolutions over the 8-year analysis period is not distinguishable from zero at the 10% significance level.

in the observations; this may be because the seasonal average in the model represents an average over many such intrusions in locations that change with time. Additionally, the surface waters are much warmer in the NARE85 observations; this is because the ocean surface was unusually ice-free in this specific part of the Weddell Sea during the period over which the measurements were conducted, whereas it is typically ice-covered in our model. At IC92 there is qualitative agreement between the model and observations, in that dense waters occupy the shelf and slope, creating an isopycnal connection between the continental shelf and the mid-depth waters offshore (Nicholls et al. 2009). However, the observed bottom waters are colder, particularly toward the bottom of the slope; this difference is likely partially inherited from the SOSE-derived eastern boundary condition in the model, but may also arise due to excessive entrainment into the dense water layer due to numerical mixing (Winton et al. 1998; Griffies et al. 2000; Legg et al. 2006). The shelf break front is also visibly sharper in the IC92 observations; this may be a result of the relatively poor constraints on the model bathymetry in this region, making it smoother than the observed sea floor.

3. Overturning circulation

In this section we quantify the overturning circulation of the southern Weddell Sea, as simulated by our regional model. The diagnostics described here will be used to decompose the overturning circulation in Section 4, and also serve as a point of comparison with previous studies. We use previously-developed frameworks to quantify the overturning circulation both in (pseudo-)latitude/density space and in temperature/salinity space; the former directly quantifies water mass transports, while the latter directly quantifies water mass transformations. We then examine the three-dimensional pathways of dense shelf water formation and export to aid interpretation of our overturning circulation diagnostics. Finally, we diagnose the temporal variability in the overturning circulation on seasonal and interannual time scales, and relate this variability to the model forcing.

a. Isopycnal overturning circulation

We first quantify the Weddell Sea overturning circulation in a space defined by a pseudo-latitudinal coordinate (discussed below) and surface-referenced potential density σ_θ, which we henceforth denote simply as σ for convenience. Using a density variable, rather than depth, as the vertical coordinate is essential to capture the various branches of the Southern Ocean overturning circulation (Döös and Webb 1994). Density-coordinate overturning calculations have therefore become standard in observational and modeling studies that emphasize the Southern Ocean (*e.g.* Hellmer and Beckmann 2001; Lumpkin and Speer 2007; Wolfe and Cessi 2009; Jullion et al. 2014; Stewart and Hogg 2017).

The choice of density variable is an important consideration in performing this calculation: ideally isopycnals should coincide as closely as possible with neutral parcel trajectories, to avoid spurious diapycnal transfers. For example, potential density referred to 2000 db is commonly used in global studies with a full, nonlinear oceanic equation of state (*e.g.* Hogg et al. 2017; Sun et al. 2020). However, in high-latitude regions, the iso-surfaces of potential density may differ substantially from neutral slopes (McDougall 1987). In the Weddell Sea, potential density typically exhibits inversions somewhere in the water column, regardless of the reference pressure used to define the density variable (see *e.g.* Stewart and Thompson 2015b). We found that surface-referenced potential density largely avoids the issue of vertical density inversions (see Fig. 4(b)). Using surface-referenced potential density also allows us to compute volume fluxes within isopycnal layers at each model time step, and save monthly time-averages of these fluxes, using MITgcm's LAYERS package. This allows us to precisely decompose the overturning circulation into contributions due to flows with different time scales of variability in Section 4.

A possible drawback of using surface-referenced potential density is that the computed streamfunction could contain artifices due to transient potential density inversions or mismatches between isopycnals of potential density and neutral slopes. An alternative approach that circumvents the limitations of potential density is to identify isopycnals by either using neutral surfaces (Nicholls et al. 2009), or by using the neutral density variable of Jackett and McDougall (1997) (*e.g.* Naveira Garabato et al. 2002; Chavanne et al. 2010; Thompson and Heywood 2008). The drawback of such density variables is that they are computationally expensive, and thus averaging fluxes within Neutral Density surfaces is typically not possible in general circulation models. Furthermore, the Neutral Density variable of Jackett and McDougall (1997) is not defined within a substantial portion of the FRIS cavity, due to a lack of available hydrographic data. In Appendix A we derive a Jackett and McDougall (1997)-like Neutral Density variable for our model domain, and show that the overturning circulation in Neutral Density space is almost identical to that derived in σ space.

Previous studies have typically used latitude as the horizontal coordinate in which to present calculations of the global overturning circulation, including the portion of that circulation that transits via the Antarctic margins (*e.g.* Lumpkin and Speer 2007; Newsom et al. 2016). However integrating longitudinally obscures the distinction between transports in different regions of the southern Weddell Sea. In particular, latitude bands often traverse both the FRIS cavity and the continental shelf, or traverse both the continental shelf and a swath of the open ocean (see Fig. 1).

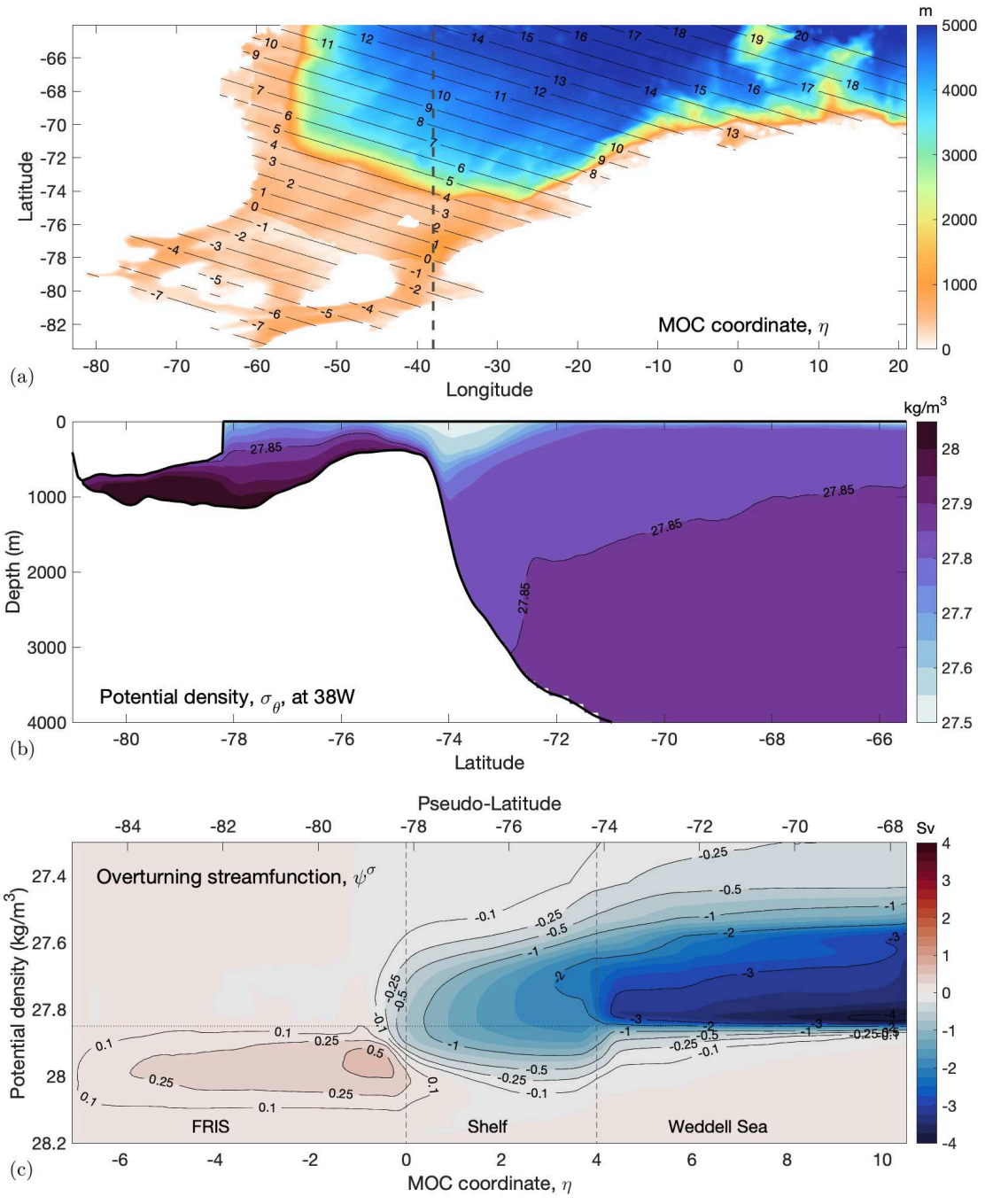

FIG. 4. Overturning circulation in density space. (a) Spatial variation of our "MOC coordinate", η (contours) and water column thickness (colours). The gray dashed line indicates 38°W, along which we plot potential density in panel (b) and convert η to a pseudo-latitude in panel (c). (b) A section along 38°W showing potential density averaged over the 8-year analysis period in our TIDES12 simulation, $\langle\overline{\sigma}\rangle$. (c) Overturning circulation in potential density space, ψ^σ, averaged over the 8-year analysis period of our TIDES12 simulation. The circulation follows streamlines clockwise around red regions and counter-clockwise around blue regions. The horizontal dotted line indicates the $\sigma = 27.85\,\mathrm{kg\,m^{-3}}$ isopycnal.

We therefore define an alternative, pseudo-latitudinal coordinate, η, in which to present the meridional overturning circulation (MOC), which we refer to as the "MOC coordinate". This coordinate is defined as

$$\eta = (\phi - \phi_0) - C_\eta \cdot (\lambda - \lambda_0), \tag{1}$$

where ϕ denotes latitude, $\phi_0 = 78.16°\text{S}$ is a reference latitude, λ denotes longitude, $\lambda_0 = 38°\text{W}$ is a reference longitude, and $C_\eta = -0.145$ defines the slopes of the iso-η lines in latitude-longitude space. The geographical variation of $\eta(\lambda, \phi)$ is shown in Fig. 4(a). We selected C_η so that $\eta = 0$ coincides approximately with the FRIS ice shelf front, while $\eta = 4$ coincides approximately with the southern Weddell Sea continental shelf break. For presentation purposes we convert η back to a "pseudo-latitude" by setting $\lambda = \lambda_0$ in (1), which simply yields the latitude at which each η isosurface intersects 38°W (see Fig. 4(a)).

Having established the pseudo-latitude/density coordinate system in which our calculations will be posed, we now discuss the formulation of the overturning ciculation. We first define the isopycnal transport below a given isopycnal surface σ,

$$\boldsymbol{U}(\boldsymbol{x}_h, \sigma, t) = \int_{z_{\text{bot}}}^{0} \boldsymbol{u}_h \mathcal{H}\left(\tilde{\sigma}(\boldsymbol{x}, t) - \sigma\right) \mathrm{d}z, \tag{2}$$

where z_{bot} denotes the elevation of the sea floor, $\boldsymbol{x}_h$ denotes the horizontal position vector, $\boldsymbol{u}_h$ denotes the horizontal velocity vector, $\tilde{\sigma}$ denotes the three-dimensional density field diagnosed from the model, and $\mathcal{H}$ denotes the Heaviside function. To compute the overturning streamfunction at a given value of η, we compute the net flux across η below the isopycnal σ,

$$\psi^\sigma(\eta, \sigma, \bar{t}) = \int_{\eta''=\eta} -\overline{\boldsymbol{U}} \cdot \hat{\boldsymbol{n}}_\eta \, \mathrm{d}s = \iint_{\eta''<\eta} -\nabla \cdot \overline{\boldsymbol{U}} \, \mathrm{d}A. \tag{3}$$

Here η'' is a variable of integration, $\mathrm{d}s$ denotes an infinitesimal distance along the contour $\eta'' = \eta$, $\mathrm{d}A$ denotes an infinitesimal horizontal area within the area defined by $\eta'' < \eta$, and $\hat{\boldsymbol{n}}_\eta$ denotes a unit vector perpendicular to η isosurfaces, pointing in the direction of positive η. The overbar denotes a monthly time-mean,

$$\overline{a} = \frac{1}{T_{\text{month}}} \int_{\text{month}} a \, \mathrm{d}t, \tag{4}$$

where the subscript month denotes an integral over an individual calendar month and T_{month} denotes the length of that month. We denote variation of monthly-averaged quantities over the months spanned by the simulation via a dependence on the monthly-mean time $\bar{t}$, to distinguish this from a dependence on continuous time t. Note that in practice we use the rightmost expression in (3) to compute ψ^σ, which is mathematically and numerically equivalent to the middle expression via the divergence theorem.

The streamfunction (3) directly quantifies isopycnal transports, but only accurately quantifies diapycnal transports when averaged over a sufficiently long period of time. To see this, note that conservation of volume beneath the isopycnal η obeys (Walin 1982; Groeskamp et al. 2019)

$$\frac{\partial \xi}{\partial t} + \nabla \cdot \boldsymbol{U} + \varpi = 0, \tag{5a}$$

$$\xi(\boldsymbol{x}_h, \sigma, t) = \int_{z_{\text{bot}}}^{0} \mathcal{H}\left(\tilde{\sigma}(\boldsymbol{x}, t) - \sigma\right) \mathrm{d}z. \tag{5b}$$

Here ξ denotes the thickness of the layer confined between the sea floor and the isopycnal σ, and $\varpi(\boldsymbol{x}_h, \sigma, t)$ denotes the diapycnal velocity across σ. Equation (5a) implies that the diapycnal velocity is only equal to the divergence of the transport $\boldsymbol{U}$ when averaged over a sufficiently long time that $\partial\xi/\partial t$ becomes negligible. We therefore present the majority of our overturning diagnostics as averages over the full 8-year analysis period. We denote these multi-decadal averages using angle brackets,

$$\left\langle a\left(\bar{t}\right)\right\rangle = \frac{1}{T_{\text{sim}}} \int_{\text{sim}} a\left(\bar{t}\right) \mathrm{d}\bar{t}, \tag{6}$$

where the subscript $_{\text{sim}}$ denotes a time integral over the 8-year simulation analysis period, and T_{sim} denotes the simulation length. Note that this operator applies to monthly-averaged quantities, so the multi-annual time-mean of a variable b with a continuous dependence on t would be $\left\langle \overline{b(t)} \right\rangle$.

Fig. 4(c) shows the overturning streamfunction $\langle \psi^\sigma \rangle$ in our TIDES12 simulation. We divide the model domain approximately into three geographical regions: the FRIS ($\eta < 0$), the southern continental shelf ($0 < \eta < 4$) and the open Weddell Sea ($\eta > 4$). The streamfunction describes a southward transport of lighter waters ($\sigma \lesssim 27.85\,\text{kg}\,\text{m}^{-3}$) and northward return flow of denser waters ($\sigma \gtrsim 27.85\,\text{kg}\,\text{m}^{-3}$) over the continental shelf and in the open Weddell Sea. Just south of Filchner sill ($\eta \approx 3.5$), the net northward transport is approximately 1.75 Sv, which is very close to the 1.6 ± 0.5 Sv estimated by Foldvik et al. (2004). The northward transport exhibits a rapid transition at the shelf break $\eta \approx 4$, with the density of the northward-flowing waters lightening and the transport more than doubling to over 4 Sv by $\eta = 10$. This is also very close to the 4.3 ± 1.4 Sv of WSDW formation estimated by Foldvik et al. (2004). In the FRIS cavity there is an apparently separate overturning circulation that circulates in the opposite direction, with waters denser than $\sigma = 28\,\text{kg}\,\text{m}^{-3}$ flowing southward into the cavity, and lighter waters ($\sigma \approx 27.9\,\text{kg}\,\text{m}^{-3}$) returning northward. In Appendix C we show that the separation of the circulation into two overturning cells in Fig. 4(c) occurs due to a cancellation between waters crossing the same portion of η/σ space in opposite directions in different physical locations. We further show that with a suitable choice of horizontal coordinate, the two overturning cells in Fig. 4 can be collapsed into a single overturning cell. However, we opt not to take this approach because it requires a significantly

more complicated definition of the MOC coordinate, and because the FRIS overturning cell provides a useful estimate of the circulation through the FRIS cavity.

b. Thermohaline overturning circulation

To complement our diagnostics of the MOC in density space, which emphasize the isopycnal transport of water masses, we additionally diagnose the overturning circulation in temperature/salinity (θ/S) space, which directly quantifies water mass transformations. We compute the θ-S streamfunction at each point (S,θ) as (Zika et al. 2012; Döös et al. 2012),

$$\psi^{\theta S}(S,\theta,\bar{t}) = \iint_{\overline{\theta''}<\theta,\overline{S''}=S} \boldsymbol{u}^{\dagger}\cdot\hat{\boldsymbol{n}}_{\overline{S}}\,\mathrm{d}A. \tag{7}$$

Here θ'' and S'' are variables of integration, and $\hat{\boldsymbol{n}}_{\overline{S}}$ denotes a unit vector perpendicular to the (monthly-averaged) salinity field. In words, $\psi^{\theta S}$ quantifies the domain-integrated rate at which the flow crosses the salinity gradient at salinity S, wherever the temperature is lower than θ. Thus isolines of $\psi^{\theta S}$ trace the domain-averaged "pathways" of water parcels between different water masses. This streamfunction can equivalently be calculated by interchanging θ and S, with almost identical results (not shown).

We compute (7) using monthly-mean fields because the required diagnostics are not implemented in the MITgcm. Our calculation therefore omits a component of the thermohaline streamfunction associated with sub-monthly fluctuations of the flow and thermodynamic state. Following Zika et al. (2012), we therefore separately compute the overturning due to the (monthly) mean flow and due to transient flows. The velocity vector $\boldsymbol{u}^{\dagger}$ in (7) denotes the "residual" velocity (*e.g.* Plumb and Ferrari 2005), which is the sum of Eulerian-mean and "eddy"-induced components,

$$\boldsymbol{u}^{\dagger} = \overline{\boldsymbol{u}} + \boldsymbol{u}^{\star}. \tag{8}$$

We estimate the eddy-induced transport via the Neutral Temporal Residual Mean (NTRM, Stewart and Thompson 2015b; Stewart 2019), in which the eddy-induced transports are related to a streamfunction via

$$\boldsymbol{u}_h^{\star} = -\frac{\partial\boldsymbol{\psi}^{\star}}{\partial z}, \qquad w^{\star} = \nabla_h\cdot\boldsymbol{\psi}^{\star}. \tag{9}$$

The eddy streamfunction is given by

$$\boldsymbol{\psi}^{\star} = \frac{g\left(\tilde{\beta}\,\overline{\boldsymbol{u}_h' S'} - \tilde{\alpha}\,\overline{\boldsymbol{u}_h'\theta'}\right)}{N^2 + N_{\min}^2}, \tag{10}$$

where primes $'$ denote deviations from a monthly average. Here we define the mean buoyancy frequency

$$N^2 = g\left(\tilde{\beta}\,\frac{\partial\overline{S}}{\partial z} - \tilde{\alpha}\,\frac{\partial\overline{\theta}}{\partial z}\right), \tag{11}$$

and we use the notation $\tilde{\beta} = \beta(\overline{S},\overline{\theta},z)$, $\tilde{\alpha} = \alpha(\overline{S},\overline{\theta},z)$, where β is the haline contraction coefficient, and α is the thermal expansion coefficient. The quantities required to compute (10) are available as MITgcm diagnostics, provided as monthly averages over each model time step.

The NTRM was tested in an idealized model configuration with stratification based on observations from the Weddell Sea (Stewart 2019), and thus may be expected to accurately estimate eddy-induced transport in our regional model. However we found it necessary to regularize (10) via the addition of a minimum stratification $N_{\min}^2$. Without this regularization, individual gridpoints with vanishingly small vertical stratification (*e.g.* in the surface mixed layer) can produce excessively large values of $\boldsymbol{\psi}^{\star}$, which then contaminate the estimated net transport in the corresponding density surfaces. The complete NTRM contains an additional term proportional to the vertical gradient of the mean flow, $\partial\overline{\boldsymbol{u}}/\partial z$ (Stewart 2019), that is formally of the same asymptotic order as the right-hand side of (10). We neglect this term because it is also proportional to the inverse square of the buoyancy frequency, and thus makes the NTRM even more susceptible to noise in areas of weak stratification. In Appendix B we show that the eddy-induced transport computed via (10) approximately reproduces the eddy-induced transport in σ-layers diagnosed directly from the model (see Section 4).

An issue with (7) is that it must be computed in a closed domain in order to produce a closed streamfunction, whereas our model domain has open boundaries. We therefore perform an artificial closure of the circulation in our model domain by modifying the velocity field before computing (7). Specifically, we first set $\boldsymbol{u}^{\dagger}\cdot\hat{\boldsymbol{n}}_b = 0$ along the northern and eastern open boundaries of the domain. We then successively correct the velocities in the nth boundary grid cell, starting from the northwestern corner ($n = 1$). For each grid cell index, n, we first compute the volume flux convergence in that grid cell, $C_n = \iiint_{V_n}\nabla\cdot\boldsymbol{u}^{\dagger}\,\mathrm{d}V$. We then add a barotropic flow from cell n to cell $n+1$ so as to eliminate the volume flux convergence in cell n, *i.e.* we replace

$$u_{n,n+1} \to u_{n,n+1} + C_n/A_{n,n+1}, \tag{12}$$

where $u_{n,n+1}$ denotes the depth-dependent velocity normal to the interface between boundary grid cells n an $n+1$. Qualitatively, the overall result of this procedure is that water exiting the domain through the open boundary in the northwest of the domain is instead re-routed to the east, and subsequently south, along the boundary, before returning to the domain interior along the eastern boundary. We emphasize that the water mass transformations associated with this re-routing are artificial, and would change if we selected an alternative scheme for closing the thermohaline streamfunction, so care should be taken in interpreting $\psi^{\theta S}$ over the portion of (S,θ) space spanned by the water masses along the open boundaries.

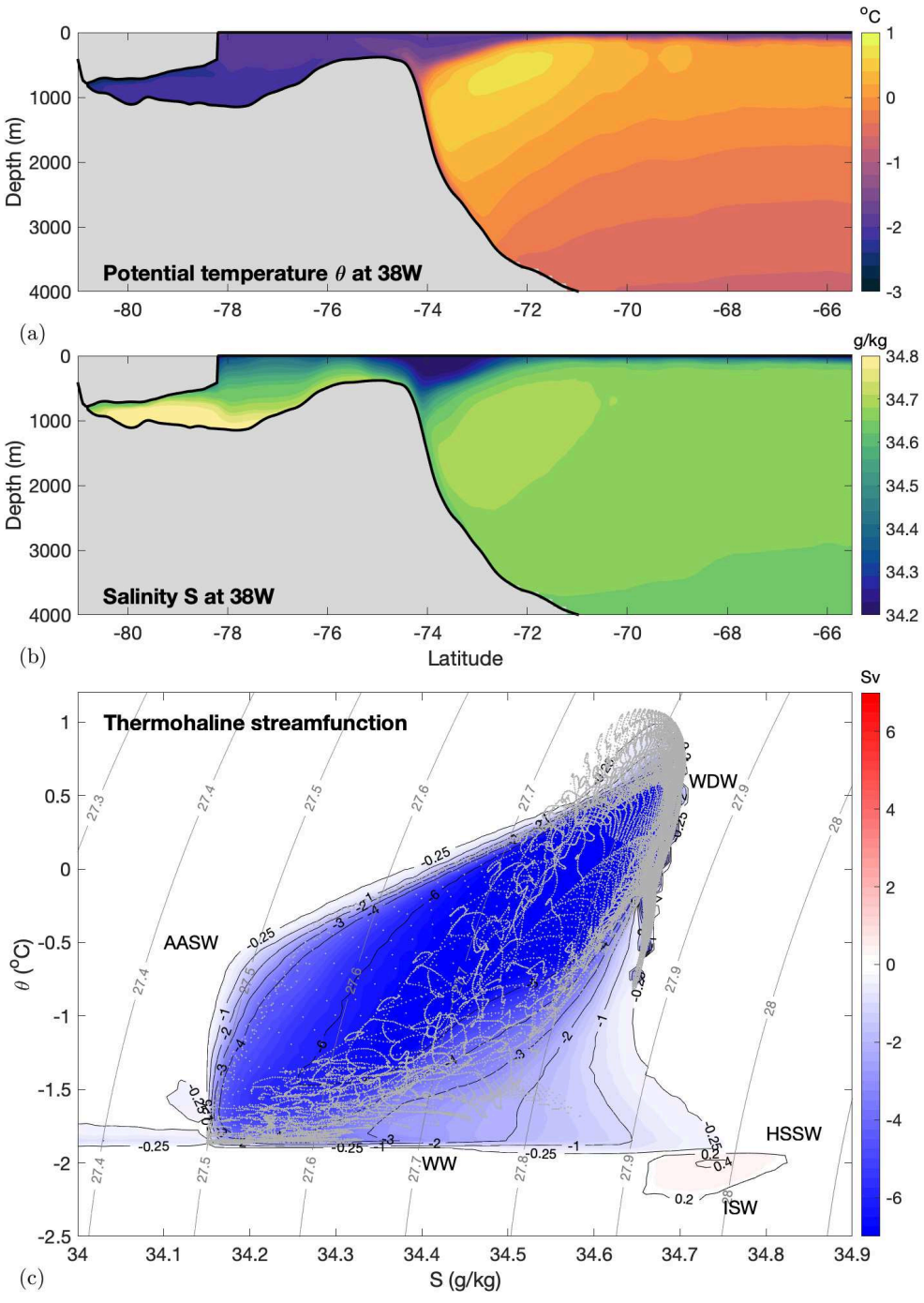

FIG. 5. (a,b) Potential temperature θ and salinity S along 38°W, and (c) thermohaline streamfunction $\psi^{\theta S}$. All panels show averages over the 8-year analysis period in our TIDES12 simulation. The gray points overlaid in panel (c) indicate the θ/S properties along the model's open boundaries, through which we impose an artificial closure of the model circulation in order to compute $\psi^{\theta S}$ (see Section 3). Text labels in panel (c) indicate the approximate properties of various previously-identified water masses, as in Fig. 3.

Fig. 5(c) shows the thermohaline streamfunction $\langle \psi^{\theta S} \rangle$, averaged over the 8-year analysis period in our TIDES12 simulation. We additionally plot sections of $\langle \overline{\theta} \rangle$ and $\langle \overline{S} \rangle$ along 38W (Fig. 5(a–b)) as a point of reference for the physical distribution of θ and S. The multi-annual mean $\langle \overline{\theta} \rangle / \langle \overline{S} \rangle$ properties along the open boundaries are overlaid

to highlight portions of S–θ space in which the streamfunction may contain artifices resulting from our closure of the model domain circulation, and thus should be interpreted with caution. The thermohaline streamfunction describes a transit of fluid parcels between water masses, the locations of which in S–θ space are marked approximately in Fig. 5(c). A transport of ~4 Sv transits from WDW via AASW through to WW, as can be seen by tracing the 4 Sv streamline through S–θ space from $(S,\theta) \approx (34.65, 0.5)$ counterclockwise to $(S,\theta) \approx (34.3, -1.9)$. At this point the streamlines diverge, similar to the divergence of the streamlines of $\langle \psi^\sigma \rangle$ at the shelf break in Fig. 4(c); the WW becomes saltier and denser to varying degrees, with a relatively small fraction of the transport transiting through HSSW (just over 1 Sv reaches a salinity higher than $34.6\,\mathrm{g\,kg^{-1}}$ at the surface freezing temperature). The streamlines then re-converge as they transit back toward WDW properties. Similar to Fig. 4(c), there is an apparently separate, clockwise overturning cell that transits between HSSW and ISW, which describes the flow of waters in the ice shelf cavity. As shown in Appendix C, this does not in fact comprise a distinct thermohaline circulation; instead water masses cross the same region of θ/S space twice: once as WW is transformed into HSSW, and again as ISW is transformed into WSDW.

c. Pathways of dense shelf water export

The key advantage of our density and thermohaline overturning streamfunctions is that they collapse information about the overturning circulation into two dimensions. However, this necessarily obfuscates some information about the three-dimensional structure of the circulation. Here we provide additional diagnostics, motivated by Figs. 4 and 5, to clarify the relationships between the streamfunctions and the three-dimensional pathways of DSW.

Fig. 4 shows that the overturning circulation on the continental shelf is primarily comprised of southward (northward) flow of waters lighter (denser) than $\sigma = 27.85\,\mathrm{kg\,m^{-3}}$. We therefore define any waters denser than $\sigma = \sigma_{\mathrm{DSW}} = 27.85\,\mathrm{kg\,m^{-3}}$ as DSW, and in Fig. 6(a) we illustrate the export pathways of DSW via a quiver plot of the transport in the DSW layer, *i.e.* $\langle \overline{\boldsymbol{U}} \rangle|_{\sigma=\sigma_{\mathrm{DSW}}}$ (see Eq. 2). The primary export pathway follows the barotropic streamlines shown in Fig 1(c): the DSW transits from the Ronne polynya via an anticyclonic circulation beneath the FRIS, and then northward along the eastern flank of Filchner Trough (see also Grosfeld and Gerdes 1998; Nicholls et al. 2009). This transit through the FRIS reinforces the artificiality of the separate FRIS overturning cell in Figs. 4 and 5 (see Appendix C). The DSW overflows across the shelf break in the Filchner Trough, as visualized by the mean thickness of the DSW layer, $\langle \xi \rangle|_{\sigma=\sigma_{\mathrm{DSW}}}$, shown Fig. 6(b). Some DSW also approaches the continental shelf break at other sites to the west of the FT, though we have not quantified this partitioning of this cross-isobath transport (see Morrison et al. 2020).

To lend insight into the process of water mass transformation that drives the circulation pathway shown in Fig. 6(a), in Fig. 6(c) we plot the time-mean diapycnal velocity $\langle \overline{\varpi} \rangle|_{\sigma=\sigma_{\mathrm{DSW}}}$, which we compute indirectly via $-\nabla \cdot \langle \overline{\boldsymbol{U}} \rangle|_{\sigma=\sigma_{\mathrm{DSW}}}$. In Fig 6(d) we plot the downward ocean surface buoyancy flux, estimated as

$$B = g\left[\alpha\left(\langle \overline{S} \rangle, \langle \overline{\theta} \rangle, z_{\mathrm{surf}}\right) \frac{\langle \overline{Q} \rangle}{\rho_0 C_p} + \beta\left(\langle \overline{S} \rangle, \langle \overline{\theta} \rangle, z_{\mathrm{surf}}\right) \frac{\langle \overline{\Sigma} \rangle \langle \overline{S} \rangle}{\rho_0}\right], \tag{13}$$

where Q is the downward surface heat flux in $\mathrm{W\,m^{-2}}$, Σ is the downward surface freshwater flux in $\mathrm{kg\,s^{-1}}$, $\rho_0 = 1027.5\,\mathrm{kg\,m^{-3}}$ is the reference density, and $C_p = 3994\,\mathrm{J\,kg^{-1}\,K^{-1}}$ is the specific heat of seawater. Both the downwelling into the DSW layer and the surface buoyancy fluxes are concentrated along the front of the FRIS, particularly in the Ronne polynya. Within the FRIS cavity there are positive and negative diapycnal velocities across $\sigma = \sigma_{\mathrm{DSW}}$ that are relatively large in magnitude, likely due to the action of surface buoyancy fluxes or lateral stirring/mixing on the relatively weak cavity stratification. Along the export pathway of DSW there is consistent, relatively strong downwelling into the DSW layer; this is consistent with the entrainment of lighter waters and intensification of the overturning streamfunction as the flow progresses northward in Figs. 4(c) and 5(c).

d. Overturning circulation variability

Finally we, briefly examine the seasonal and interannual variability in the Weddell Sea overturning circulation. Our exploration of the interannual variability is limited by the 8-year duration of the simulation analysis period. However, this quantification is necessary to provide context for Section 4, in which we quantify the contribution of seasonal/interannual variability to the multi-annual mean overturning circulation. We perform all of the following analysis using monthly calculations of the pseudo-latitude/density streamfunction ψ^σ because this streamfunction allows us to relate the variability to different geographical regions.

In Figs. 7(a–b) we plot the standard deviation of ψ^σ over the 8-year analysis period. We separately consider the variability including (Fig. 7(a)) and excluding (Fig. 7(b)) the mean seasonal cycle, in order to distinguish seasonal and interannual variability. Figs. 7(c–d) show the time-varying strength of the overturning circulation. We quantify the strength of the overturning circulation via

$$\Psi_{\max}(t) = \max_{\eta,\sigma}\{|\psi^\sigma|\}. \tag{14}$$

This metric obscures information about the strength of the overturning over the continental shelf and slope, which

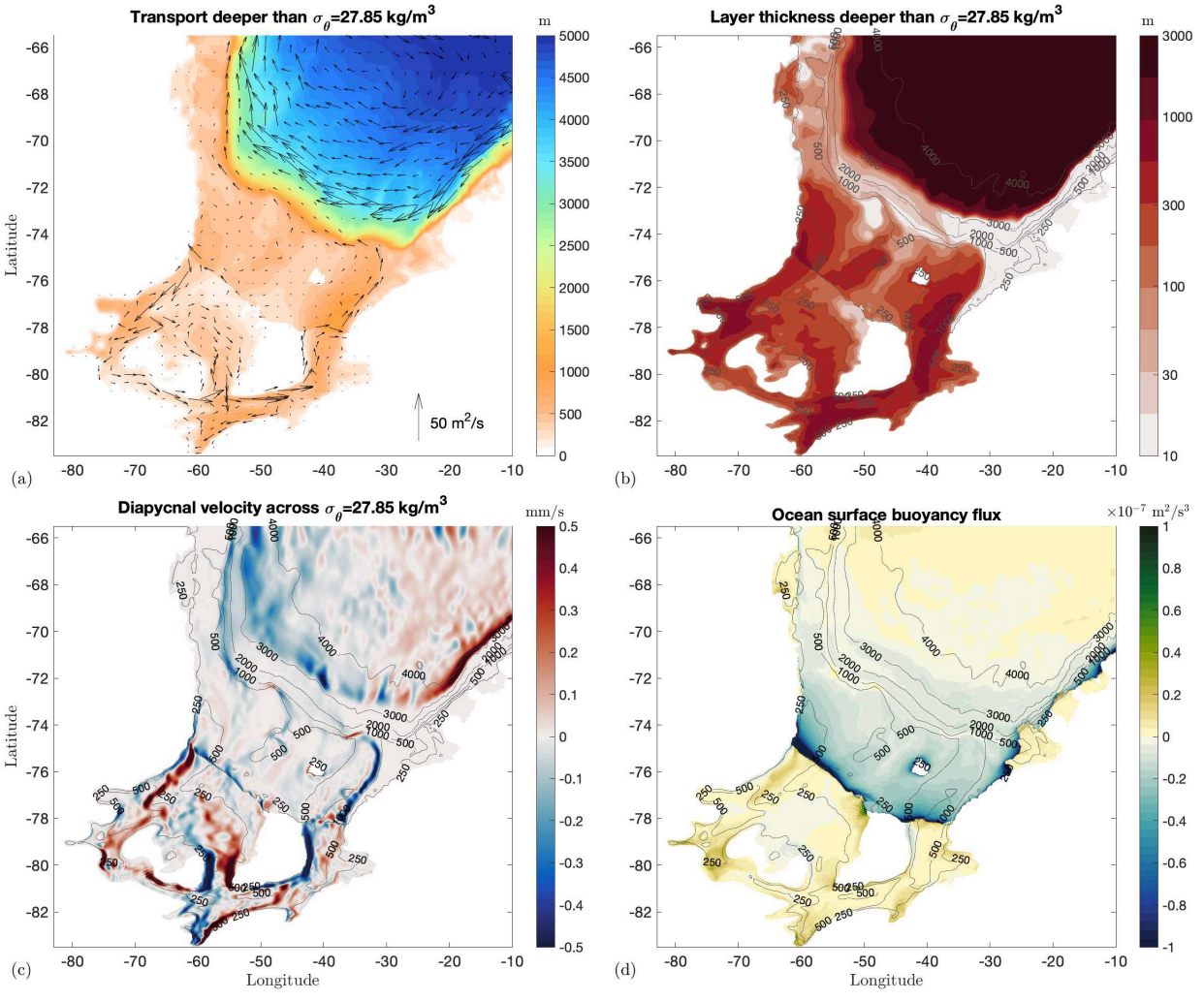

FIG. 6. Three-dimensional structure of the formation and export of dense shelf water (DSW) from the southern Weddell Sea continental shelf in our TIDES12 simulation. (a) Time-averaged transport in the DSW layer, $\langle \overline{\boldsymbol{U}} \rangle|_{\sigma_\theta=27.85\,\mathrm{kg\,m^{-3}}}$. (b) Mean thickness, $\langle \overline{\xi} \rangle$, of the DSW layer. (c) Mean upward diapycnal velocity, $\langle \overline{\varpi} \rangle$, across the upper surface of the DSW layer. (d) Mean downward buoyancy flux across the ocean surface, B, including the portions of the domain that lie below ice shelves. Note that these fluxes are capped at $\pm 10^{-7}\,\mathrm{m^2\,s^{-3}}$ to improve the clarity of the plot, but the fluxes locally exceed $-5\times10^{-7}\,\mathrm{m^2\,s^{-3}}$ in regions such as the Ronne polynya. Water column thickness in meters is shown in contours in panels (b–d) and in colors in panel (a).

is weaker on average (Fig. 4) and has a smaller standard deviation (Fig. 7). We therefore define metrics that are analogous to (14), but which specifically quantify the overturning strengths on the continental shelf,

$$\Psi_{\mathrm{shelf}} = -\min_{0<\eta<3.5,\,\sigma} \{\psi^\sigma\}. \tag{15}$$

and in the FRIS cavity,

$$\Psi_{\mathrm{cavity}} = \max_{\eta<0,\,\sigma} \{\psi^\sigma\}. \tag{16}$$

We use $\eta = 3.5$ as the northern edge of the continental shelf for this calculation because the entrainment of offshore water masses has already begun by $\eta = 4$, visible in Fig. 4(c).

Figs. 7(a–b) show that the overturning exhibits variability across the entire model domain, with amplitudes typically on the same order of magnitude as the mean overturning circulation (Fig. 4). The the seasonal cycle is most prominent in the open Weddell Sea, in the ~24.5–26.5 $\mathrm{kg\,m^{-3}}$ density range, where it produces a very large (3–4 Sv) fluctuation in the streamfunction (Fig. 7(a)). This leads to large seasonal variations in Ψ_{max}, ranging from 3–5 Sv in austral winter/spring to 8–10 Sv in austral summer and fall (Fig. 7(c)). We speculate that this is primar-

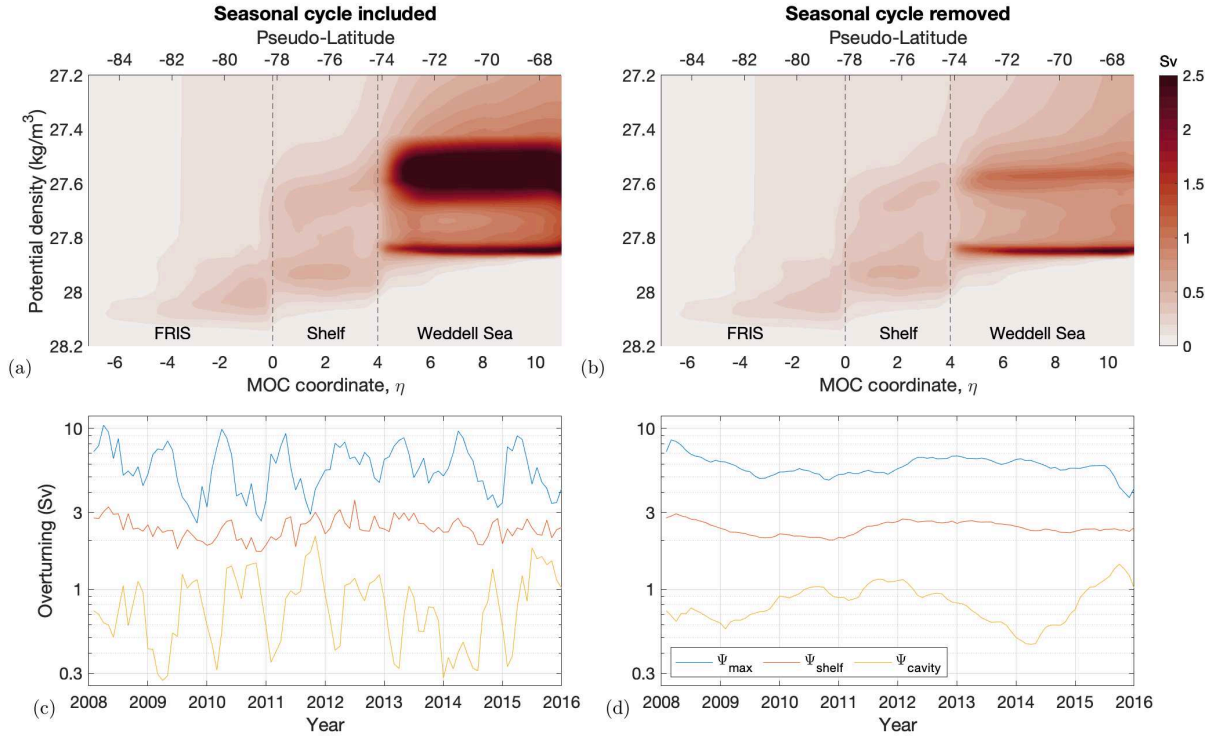

FIG. 7. Diagnostics of variability in the overturning streamfunction in density space, ψ^σ, in our TIDES12 simulation (a,c) with and (b,d) without the mean seasonal cycle included. (a,b) Month-to-month standard deviation of the overturning streamfunction in density space, ψ^σ. (c,d) Time series of the maximum overturning strength $\Psi_{\max}$ (14), the continental shelf overturning strength Ψ_{shelf} (15), and the FRIS cavity overturning strength Ψ_{cavity} (16). In panel (d) the time series have all been smoothed via a 12-month running mean in order to isolate the interannual variability from sub-seasonal variability.

ily associated with a seasonal cycle in the density of the surface waters that are transported southwestward toward the southern Weddell Sea continental shelf (Graham et al. 2013). Fig. 7(c) shows that the cavity overturning Ψ_{FRIS} also exhibits a relatively strong seasonal cycle, ranging from ~0.5 Sv in summer to 1–2 Sv in winter. This timing is consistent with the seasonal cycle of surface buoyancy loss, which is strongest in winter (Nicholls et al. 2009). In contrast, the overturning circulation on the continental shelf exhibits very little discernible seasonal variability (Fig. 7(c)). It is unclear why variations in the cavity overturning strength, presumably driven by variations in HSSW production, do not translate to variations in DSW transport across the continental shelf. Fig. 7(d) shows that $\Psi_{\max}$, Ψ_{shelf} and Ψ_{cavity} all exhibit interannual variability, with standard deviations of approximately 0.8 Sv, 0.2 Sv and 0.2 Sv, respectively. These time series hint at a lagged relationship, with interannual intensification of the cavity overturning leading that of the shelf and subsequently the open ocean, but our model does not simulate a sufficiently long time period to test such relationships.

4. Roles of tides, eddies and seasonal/interannual variability

In Section 3 we quantified the Weddell Sea MOC using streamfunctions that separately emphasize water mass transport and transformation, and characterized the three-dimensional pathways and variability of DSW export. We now aim to distinguish the roles of different processes, specifically tides, eddies and seasonal/interannual variability, in driving these water mass transports and transformations. Note that we use "eddies" as a catch-all for all non-tidal flows occurring on sub-monthly time scales, which includes various topographic and shelf waves (*e.g.* Marques et al. 2014; Daae et al. 2019; Spence et al. 2017) as well as mesoscale eddies. Later in this section we provide evidence that the "eddies" are, in fact, baroclinically-generated mesoscale eddies associated with the Filchner overflow.

a. Decomposition of the isopycnal overturning circulation

We first partition the MOC in density space into contributions from mean flows, seasonal/interannual fluctua-

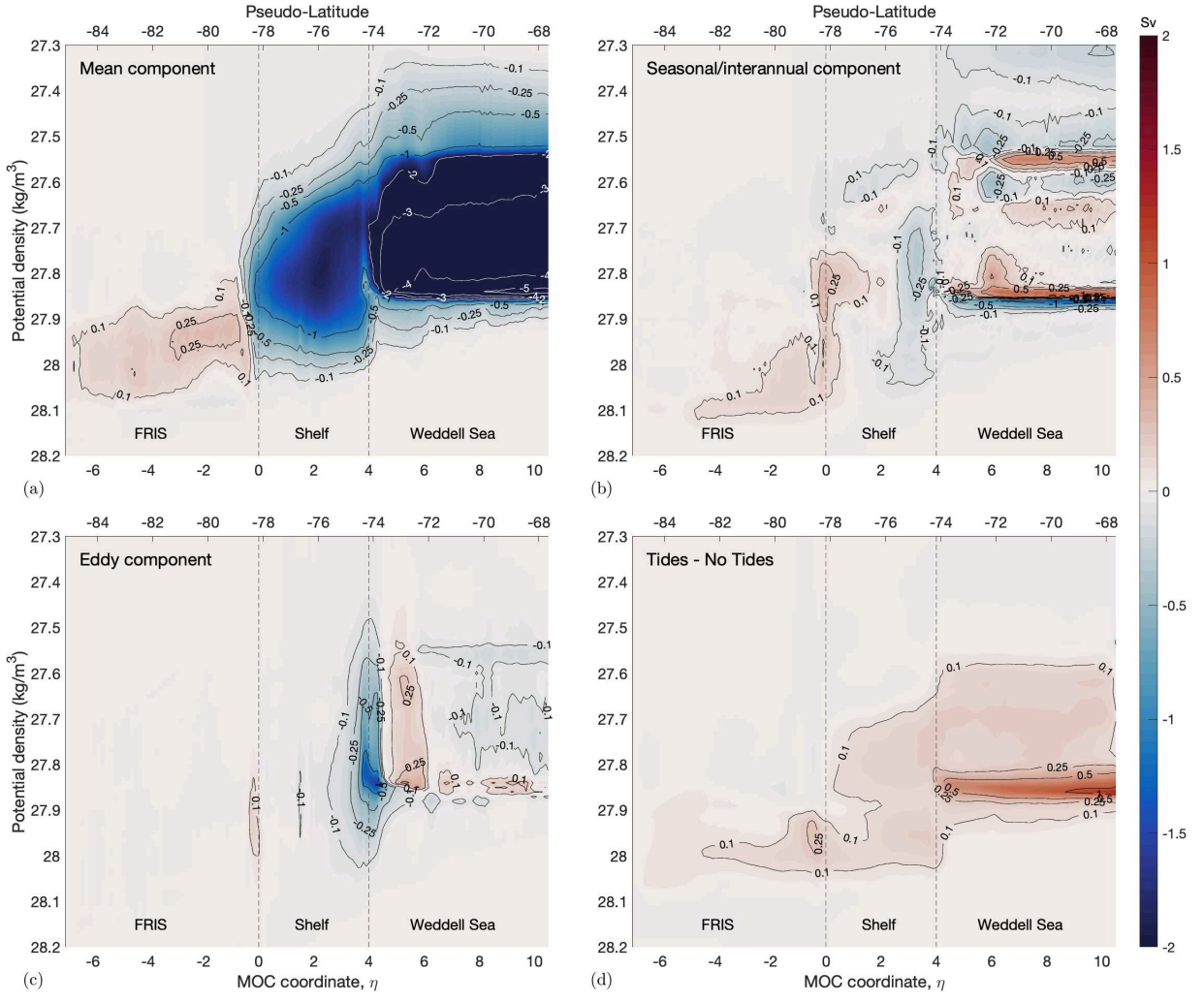

FIG. 8. Decomposition of the Weddell Sea overturning circulation in pseudo-latitude/density space into contributions from (a) multi-annual mean flows, (b) seasonal/interannual fluctuations, and (c) eddies/sub-monthly variability, and (d) difference in the overturning circulation due to the inclusion of tides (see Section 4). Panels (a–c) are derived from our NOTIDES12 simulation, such that the sum of panels (a–d) is exactly equal to the TIDES12 streamfunction shown in Fig. 4(c).

tions, and eddies. We pose a decomposition of the multi-annual mean streamfunction as

$$\langle \psi^\sigma \rangle = \psi^\sigma_{\text{mean}} + \left\langle \psi^\sigma_{\text{fluc}} \right\rangle + \left\langle \psi^\sigma_{\text{eddy}} \right\rangle, \tag{17}$$

where $\psi^\sigma_{\text{mean}}$, $\psi^\sigma_{\text{fluc}}$ and $\psi^\sigma_{\text{eddy}}$ denote the mean, seasonal/interannual and eddy components of the streamfunction, respectively. The streamfunction components are computed analogously to (3), using the following transport velocities:

$$\boldsymbol{U}_{\text{mean}}(x,y,\sigma) = \int_{z_{\text{bot}}}^{0} \langle \overline{\boldsymbol{u}_h} \rangle \, \mathcal{H}\left(\langle \overline{\tilde{\sigma}} \rangle - \sigma \right) \mathrm{d}z, \tag{18a}$$

$$\boldsymbol{U}_{\text{fluc}}(x,y,\sigma,\bar{t}) = \int_{z_{\text{bot}}}^{0} \overline{\boldsymbol{u}_h} \, \mathcal{H}\left(\overline{\tilde{\sigma}} - \sigma \right) \mathrm{d}z \; - \; \boldsymbol{U}_{\text{mean}}, \tag{18b}$$

$$\boldsymbol{U}_{\text{eddy}}(x,y,\sigma,\bar{t}) = \overline{\boldsymbol{U}} \; - \; \boldsymbol{U}_{\text{fluc}} \; - \; \boldsymbol{U}_{\text{mean}}. \tag{18c}$$

In words, $\boldsymbol{U}_{\text{mean}}$ quantifies multi-annual mean volume fluxes within multi-annual mean density surfaces, $\boldsymbol{U}_{\text{fluc}}$ quantifies seasonal/interannual fluctuations of monthly-mean volume fluxes within monthly-mean density surfaces,

and $\boldsymbol{U}_{\text{eddy}}$ quantifies sub-monthly correlations between instantaneous isopycnal flows and instantaneous isopycnal layer thicknesses. This approach is standard for decomposing mean and eddy fluxes in isopycnal coordinates (*e.g.* Stewart and Thompson 2013; Wolfe 2014); (18a)–(18c) simply constitutes an extension to three different time scales of variability. A caveat to this decomposition is that any flow in density classes denser than the monthly-mean density at the sea floor (or lighter than the monthly-mean density at the surface) is necessarily included in the "eddy" component.

In Fig. 8(a–c) we plot the mean, seasonal/interannual and eddy components of the overturning streamfunction (17) in our NOTIDES12 simulation. To quantify the impact of tides, in Fig. 8(d) we plot the difference in $\langle \psi^{\sigma} \rangle$ between our TIDES12 and NOTIDES12 simulations; thus the sum of panels (a–d) in Fig. 8 is identical to Fig. 4(c). In density space the overturning is dominated by the time-mean transport, as $\psi^{\sigma}_{\text{mean}}$ closely resembles the full overturning $\langle \psi^{\sigma} \rangle$ in Fig. 4(c). Seasonal/interannual variability serves to strengthen the cavity overturning by approximately 0.15 Sv, while also increasing the density of the densest northward-flowing waters in the open Weddell Sea. Note that diagnosing the seasonal/interannual component of the overturning in the TIDES12 simulation, rather than the NOTIDES12 simulation, yields an almost identical result (not shown). The eddy component of the overturning plays a more substantial role, albeit localized to the continental shelf break ($\eta \approx 4$). To quantify the eddy contribution, we consider the transport where the eddy streamfunction reaches its maximum of 1.68 Sv, at $\eta = 4.3$. At this pseudo-latitude, the total offshore transport in the NOTIDES12 simulation is 3.24 Sv, and this transport occurs at densities greater than $\sigma_\theta = 27.81\,\text{kg}\,\text{m}^{-3}$. The net offshore transport by eddies at densities greater than $\sigma_\theta = 27.81\,\text{kg}\,\text{m}^{-3}$ is 1.12 Sv, which corresponds to 35% of the total transport. However, of the 3.24 Sv total transport across $\eta = 4.3$, most (2.80 Sv) occurs at densities greater than $\sigma_\theta = 27.84\,\text{kg}\,\text{m}^{-3}$, which corresponds to the maximum of the eddy streamfunction. Thus eddies export 60% of the waters denser than $\sigma_\theta = 27.84\,\text{kg}\,\text{m}^{-3}$, which in turn comprise 86% of the total dense water export.

The addition of tides serves to strengthen the cavity overturning circulation substantially, by around 0.2 Sv, while weakening the export of dense water across the continental shelf by approximately 0.2 Sv, and decreasing the density of the WSDW exported northward in the open Weddell Sea. We quantify these changes later in this section; note that these measures are not sensitive to small changes in the density threshold used to define the DSW layer. Note also that the "eddy" component of the overturning has a very similar structure with or without tides (not shown), which strongly suggests that tides are not producing any substantial rectified water mass transport. We quantify the difference in the eddy overturning strengths in simulations with and without tides later in this section. Rather, Fig. 8 suggests that tides primarily influence the overturning circulation by increasing the FRIS melt rate (see Fig. 2), thus reducing the net buoyancy loss over the continental shelf and lightening the exported dense shelf waters.

b. Decomposition of the thermohaline circulation

In Fig. 9 we perform an analogous decomposition of our thermohaline streamfunction $\psi^{\theta S}$,

$$\left\langle \psi^{\theta S} \right\rangle = \psi^{\theta S}_{\text{mean}} + \left\langle \psi^{\theta S}_{\text{fluc}} \right\rangle + \left\langle \psi^{\theta S}_{\text{eddy}} \right\rangle. \tag{19}$$

The mean, seasonal/interannual and eddy components are defined analogously to (18a)–(18c), except in this case the eddy component is estimated directly from the NTRM velocity $\boldsymbol{u}^{\star}$,

$$\psi^{\theta S}_{\text{mean}}(S,\theta) = \iint_{\langle \overline{\theta''} \rangle < \theta, \langle \overline{S''} \rangle = S} \langle \overline{\boldsymbol{u}} \rangle \cdot \hat{\boldsymbol{n}}_{\langle \overline{S} \rangle} \, \mathrm{d}A, \tag{20a}$$

$$\psi^{\theta S}_{\text{fluc}}(S,\theta,\bar{t}) = \iint_{\overline{\theta''} < \theta, \overline{S''} = S} \overline{\boldsymbol{u}} \cdot \hat{\boldsymbol{n}}_{\overline{S}} \mathrm{d}A \; - \; \psi^{\theta S}_{\text{mean}}, \tag{20b}$$

$$\psi^{\theta S}_{\text{eddy}}(S,\theta,\bar{t}) = \iint_{\overline{\theta''} < \theta, \overline{S''} = S} \boldsymbol{u}^{\star} \cdot \hat{\boldsymbol{n}}_{\overline{S}} \mathrm{d}A. \tag{20c}$$

Here the notation extends that of (7): for example $\hat{\boldsymbol{n}}_{\langle \overline{S} \rangle}$ denotes a unit vector normal to the multi-annual mean salinity field. The interpretation of (20a)–(20c) is analogous to that of (18a)–(18c): $\psi^{\theta S}_{\text{mean}}$ quantifies water mass transformations due to multi-annual mean flows across multi-annual mean θ/S gradients, $\psi^{\theta S}_{\text{fluc}}$ quantifies seasonal/interannual fluctuations in the monthly-mean flows across monthly-mean θ/S gradients, and $\psi^{\theta S}_{\text{eddy}}$ quantifies eddy-induced transports across monthly-mean θ/S gradients. Note that the total thermohaline overturning $\left\langle \psi^{\theta S} \right\rangle$ in (19) differs slightly from streamfunction that would be obtained by averaging the thermohaline transports over every model time step, rather than using the NTRM to estimate the submonthly component, as discussed in Section 3.

Similar to our decomposition of the overturning in density space, the mean streamfunction from the NOTIDES12 simulation (Fig. 9(a)) qualitatively resembles the total overturning circulation $\left\langle \psi^{\theta S} \right\rangle$, shown in Fig. 5(c). The overturning driven by seasonal/interannual fluctuations (Fig. 9(b)) is visibly noisy, and exhibits some qualitative differences from Fig. 8(b). For example, whereas seasonal/interannual fluctuations slightly strengthen the cavity overturning in density space, they slightly weaken the cavity overturning in θ/S space. Seasonal/interannual fluctuations also do not visibly increase the density of the DSW exported from the continental shelf in θ/S space, in contrast with Fig. 8(b). The eddy component of the thermohaline overturning (Fig. 9(c)) spans a large portion of θ–S space, and plays a key role in the transit between WW, HSSW and offshore water masses. In particular, the eddies and

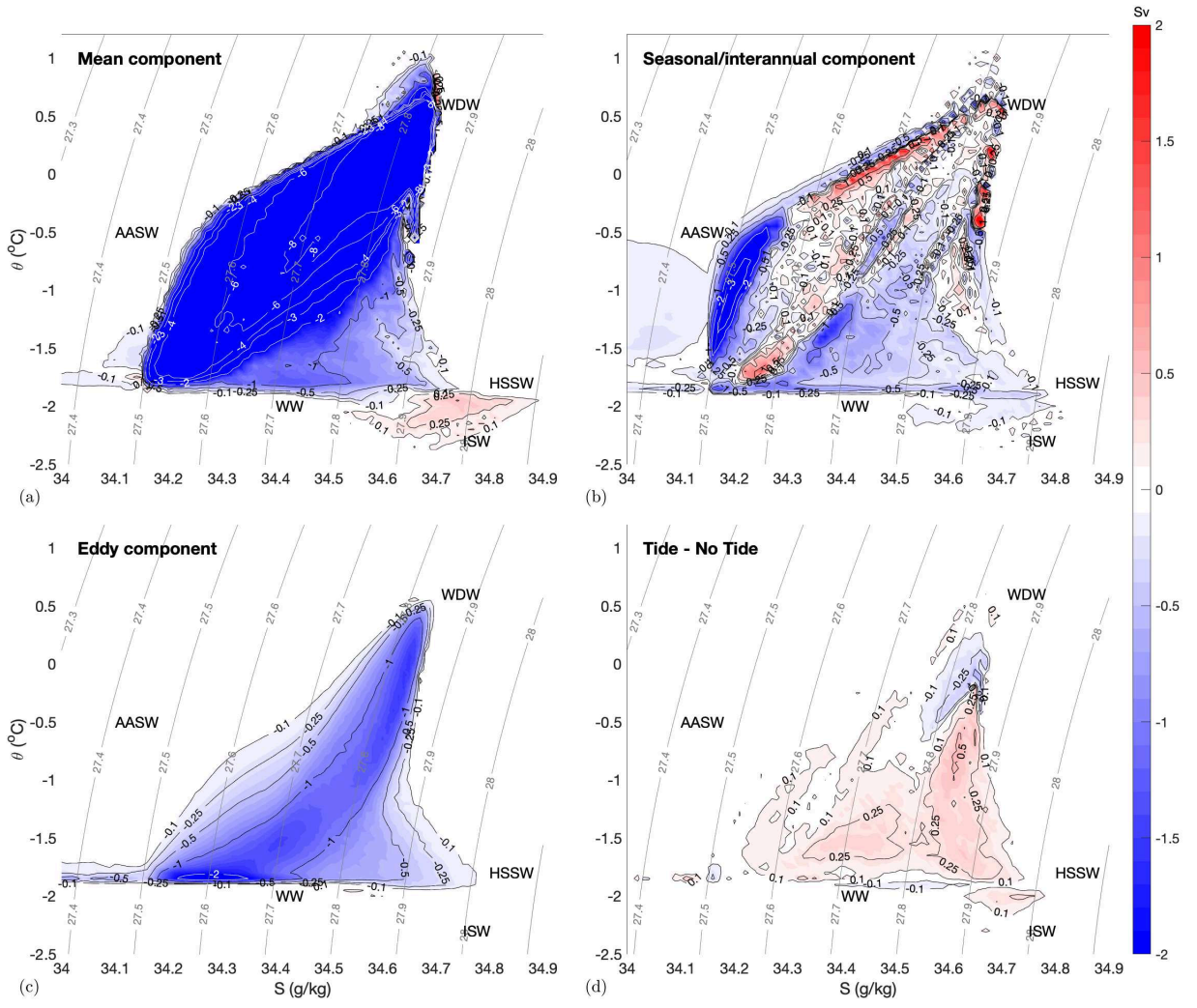

FIG. 9. Decomposition of the Weddell Sea overturning circulation in temperature/salinity space into contributions from (a) multi-annual mean flows, (b) seasonal/interannual fluctuations, and (c) eddies/sub-monthly variability, and (d) difference in the overturning circulation due to the inclusion of tides (see Section 4). Panels (a–c) are derived from our NOTIDES12 simulation, such that the sum of panels (a–d) is exactly equal to the TIDES12 streamfunction shown in Fig. 5(c). Note that we have limited the color range to -2 to +2 Sv; where the magnitude of the streamfunction exceeds this range we plot additional streamlines using white contours.

mean flow play comparable roles in the export and transformation of the densest shelf waters (HSSW and ISW), consistent with Fig. 8(c). The response of the overturning to the inclusion of tides (Fig. 9(d)) is similar to that shown in Fig. 8(d): the tides strengthen the cavity water mass transformation by approximately 0.2 Sv and weaken the overall export of dense shelf waters by around 0.25 Sv.

c. *Decomposition of quasi-meridional heat and salt fluxes*

Being a buoyancy-driven circulation, the Weddell Sea overturning is necessarily associated with transfers of heat and salt between the open ocean, continental shelf and FRIS cavity. To provide further insight into the relative roles of mean flows, seasonal/interannual fluctuations, eddies and tides in driving these transfers we decompose the quasi-meridional heat and salt fluxes as

$$F^{\chi}(\eta) = F^{\chi}_{\text{mean}} + F^{\chi}_{\text{fluc}} + F^{\chi}_{\text{eddy}}. \tag{21}$$

Here $\chi = \theta$ for the heat flux or or $\chi = S$ for the salt flux. The mean, fluctuating and eddy components of the χ-flux

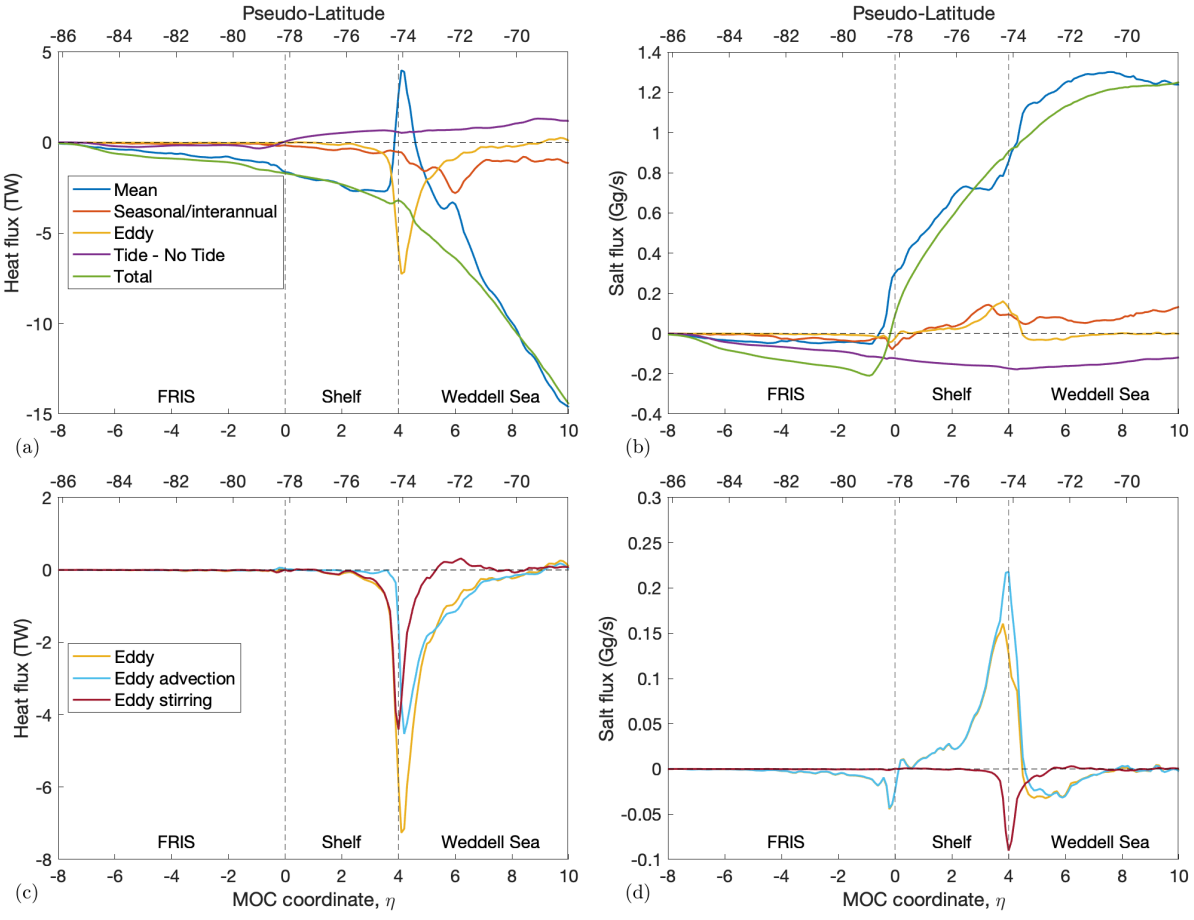

FIG. 10. Pseudo-meridional fluxes of (a,c) heat and (b,d) salt in our regional model, with positive values corresponding to northward fluxes. (a,b) Decomposition of the fluxes into contributions from multi-annual mean flows, seasonal/interannual fluctuations, and eddies/sub-monthly variability in our NOTIDES12 simulation, and difference in the fluxes due to the inclusion of tides (see Section 4). (c,d) Decomposition of the eddy fluxes into contributions due to eddy-induced advective transport and eddy isopycnal stirring.

are defined as

$$F^{\mathcal{X}}_{\text{mean}}(\eta) = \int_{\eta''=\eta} \mathrm{d}s \int_{z_{\text{bot}}}^{0} \mathrm{d}z \, \langle \overline{\chi} \rangle \, \langle \overline{\boldsymbol{u}_h} \rangle \cdot \hat{\boldsymbol{n}}_\eta, \tag{22a}$$

$$F^{\mathcal{X}}_{\text{fluc}}(\eta) = \int_{\eta''=\eta} \mathrm{d}s \int_{z_{\text{bot}}}^{0} \mathrm{d}z \, \langle \overline{\chi}\,\overline{\boldsymbol{u}_h} \rangle \cdot \hat{\boldsymbol{n}}_\eta - F^{\mathcal{X}}_{\text{mean}}, \tag{22b}$$

$$F^{\mathcal{X}}_{\text{eddy}}(\eta) = \int_{\eta''=\eta} \mathrm{d}s \int_{z_{\text{bot}}}^{0} \mathrm{d}z \, \left\langle \overline{\chi' \boldsymbol{u}'_h} \right\rangle \cdot \hat{\boldsymbol{n}}_\eta. \tag{22c}$$

In words, $F^{\mathcal{X}}_{\text{mean}}$ quantifies advection of the multi-annual mean tracer by the multi-annual mean flow, $F^{\mathcal{X}}_{\text{fluc}}$ quantifies seasonal/interannual fluctuations in tracer advection by seasonal/interannual perturbations to the monthly-mean flow, and $F^{\mathcal{X}}_{\text{eddy}}$ quantifies tracer advection due to correlations between sub-monthly tracer and velocity fluctuations.

In Fig. 10(a–b) we plot this decomposition of the heat and salt fluxes for the NOTIDES12 simulation, and quantify the impact of tides via the difference in $F^{\mathcal{X}}$ between the TIDES12 and NOTIDES12 simulations. Note that all freshwater fluxes are represented as virtual salt fluxes in the model, so the salt fluxes in Fig. 10(b) can be directly converted to a freshwater flux. While the net heat flux is consistently shoreward, the salt flux is offshore over the continental shelf and in the open Weddell Sea and shoreward in the FRIS cavity. The net heat and salt fluxes are dominated by the multi-annual mean flows, with two key exceptions: (i) in the FRIS cavity the shoreward salt flux is due to mean flows and seasonal/interannual fluctuations, and is substantially increased by the inclusion of tides (Mueller et al. 2018; Hausmann et al. 2020), and (ii) the shoreward heat flux across the shelf break ($\eta \approx 4$) is entirely driven by eddies. In fact, the mean heat flux changes sign at the shelf break, locally being directed offshore. This occurs because eddies largely take over the export of the densest waters at the shelf break (see $\eta \approx 4$

in Fig. 8(c)), shifting the offshore transport by the mean flow to lighter densities (see $\eta \approx 4$ Fig. 8(a)). Thus the mean overturning locally transfers cold near-surface waters shoreward while exporting warmer MWDW, which corresponds to an offshore heat transport across the shelf break. By contrast, eddies contribute only modestly to the salt flux across the shelf break (17% of the total salt flux at $\eta = 4$), seasonal/interannual variability modestly increases shoreward heat flux and offshore salt flux (16% and 10% of the total fluxes at $\eta = 4$, respectively), and inclusion of tides modestly decreases offshore heat flux and shoreward salt flux (19% of the total heat and salt fluxes at $\eta = 4$). This is consistent with the modest contributions of the seasonal/interannual variability and tides to the overturning streamfunction in Figs. 8 and 9.

d. Role and generation of mesoscale eddies

Figs. 8 and 9 suggest that, of the different forms of variability considered in this study, eddies play a particularly significant role in the export and transformation of DSW, and in the transfer of heat onto the continental shelf. These contributions are primarily associated with the overflow of DSW at the mouth of the Filchner trough (Darelius et al. 2009; Daae et al. 2018). We therefore now provide further exposition of the role of eddies in transport of heat and salt toward the FRIS. We additionally provide diagnostics of the eddy-induced transport and sources/sinks of eddy energy, which support our association attribution of the sub-monthly component of the simulated variability to mesoscale eddies.

We first note that mesoscale eddies are recognized to have two major effects on ocean tracer distributions: stirring of tracers along density surfaces and a generalized Stokes drift advection (Gent and McWilliams 1990; Plumb and Ferrari 2005). To approximately distinguish these effects, we further decompose the quasi-meridional heat and salt fluxes into eddy advective fluxes and eddy stirring fluxes following Stewart and Thompson (2016) and Stewart et al. (2018),

$$F^{\chi}_{\text{adv}} = \int_{\eta''=\eta} \mathrm{d}s \int_{z_{\text{bot}}}^{0} \mathrm{d}z \, \langle \overline{\chi}\, \boldsymbol{u}^{\star}_h \rangle \cdot \hat{\boldsymbol{n}}_{\eta}, \tag{23}$$

$$F^{\chi}_{\text{stir}} = F^{\chi}_{\text{eddy}} - F^{\chi}_{\text{adv}}. \tag{24}$$

Here again $\chi = \theta$ for heat fluxes and $\chi = S$ for salt fluxes. Fig. 10(c–d) shows that while eddy advection is primarily responsible for the flux of salt across the shelf break, eddy advection and stirring play comparable roles in the transfer of heat across the shelf break. This is consistent with salinity primarily controlling the buoyancy gradients, with temperature being a relatively passive tracer, and is consistent with previous studies that have found eddy stirring to play a key role in driving heat onto the Antarctic continental shelf (Stewart and Thompson 2016; Stewart et al. 2018).

Fig. 11(a) visualizes this eddy advection/stirring of heat onto the continental shelf via a snapshot of potential temperature at 340m depth. The Antarctic Slope Front is visible as an abrupt change in potential temperature from offshore ($\theta \approx 0.5\,^{\circ}$C) to the near freezing temperature ($\theta \approx -1.8\,^{\circ}$C). mWDW ($\theta \approx -0.5\,^{\circ}C$) is transported shoreward under the Antarctic Slope Front and onto the continental shelf everywhere to the west of Filchner Trough. The continental slope immediately to the west of Filchner Trough also hosts elevated eddy activity, as can be discerned from a snapshot of the depth-averaged vortex Rossby number $\mathrm{Ro} = (\nabla \times \boldsymbol{u}_h)/f$ (Fig. 11(b)). More quantitatively, in Fig. 11(d) we plot the eddy kinetic energy (EKE), averaged over the 8-year analysis period and over the water column depth,

$$\mathrm{EKE} = \tfrac{1}{2} \left\langle \overline{\boldsymbol{u}'^{\,2}_h} \right\rangle. \tag{25}$$

We diagnose eddy statistics from the NOTIDES12 simulation because in the TIDES12 simulation the tidal kinetic energy dominates at sub-monthly time scales, and thus obscures the energy in the eddy field. The EKE is enhanced along the continental slope to west of Filchner Trough, and along the front of the FRIS, with the very largest values $\sim 0.1\,\mathrm{m^2\,s^{-2}}$ occurring at the mouth of Filchner Trough. These horizontal distributions of eddy activity and temperature anomalies are consistent with the eddy-driven onshore transport of heat anomalies across the shelf break diagnosed in Fig. 10.

The enhancement of the eddy energy along the continental slope also coincides with the locations of eddy-induced velocity in the DSW layer. Fig. 11(c) shows the direction and magnitude of the multi-annual mean eddy-induced velocity in the DSW layer,

$$\boldsymbol{u}_{\text{eddy}} = \frac{\boldsymbol{U}_{\text{eddy}}|_{\sigma=\sigma_{\text{DSW}}}}{\overline{\xi}_{\sigma=\sigma_{\text{DSW}}}}. \tag{26}$$

The eddy-induced velocity is concentrated along the southern Weddell Sea continental slope, and is primarily directed along-slope (westward), with a weaker downslope component that is most pronounced close to Filchner Trough. Note that we show the eddy-induced velocity in Fig. 11(c), *i.e.* the transport averaged over the depth of the DSW layer, because we expect its spatial patterns to be comparable to other depth-averaged properties, such as those in Figs. 11(b) and 11(d). The collocation of the eddy-driven export of DSW and the import of mWDW is consistent with the mechanism proposed by Stewart and Thompson (2016) and Morrison et al. (2020), in which the down-slope flow of DSW transfers momentum upward into the overlying WDW layer, driving a shoreward transport of WDW.

This mechanism is further supported by a consideration of the EKE budget (Figs. 11(e–f)), which indicates that

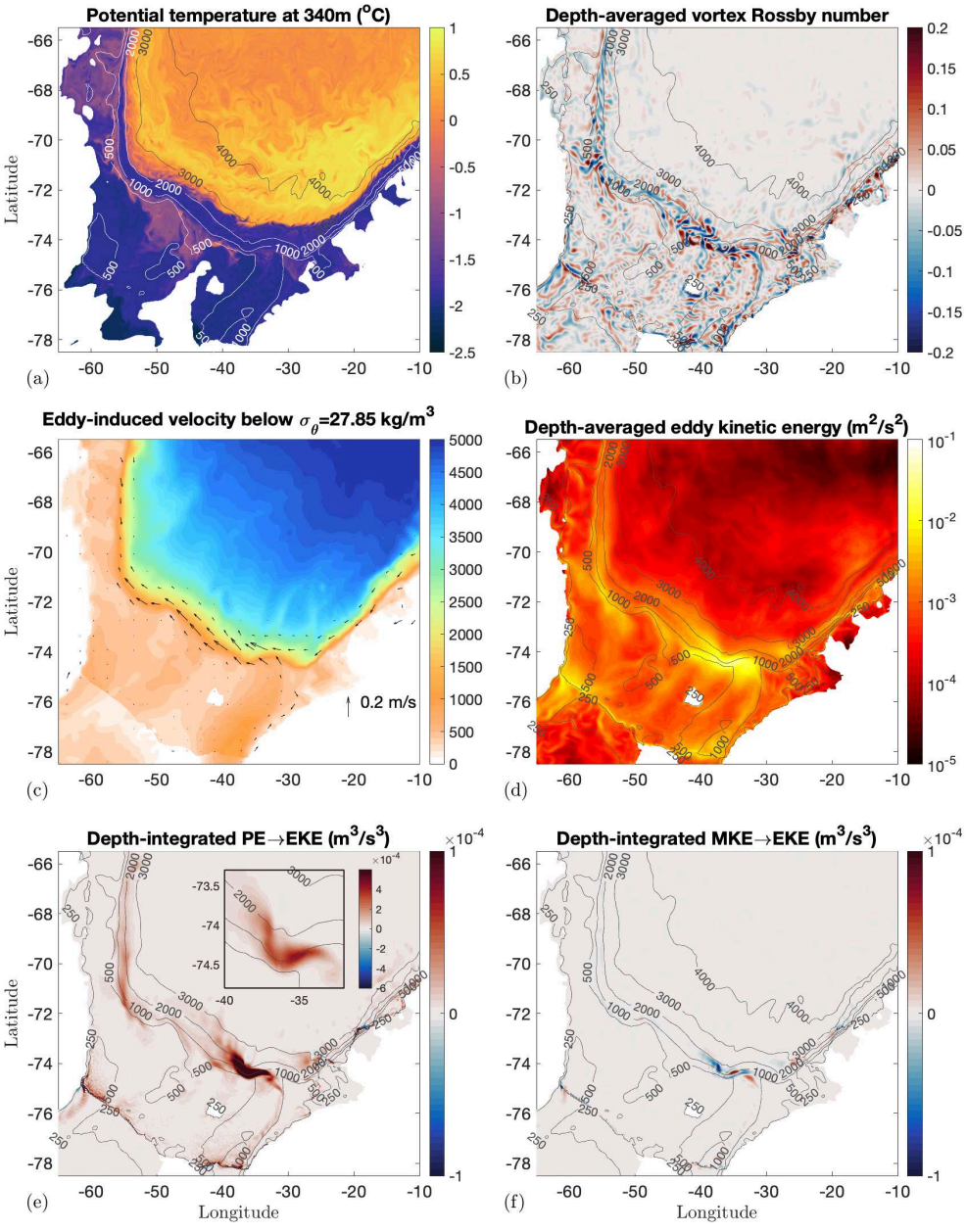

FIG. 11. Role and generation of eddies over the southern Weddell Sea continental shelf in our NOTIDES12 simulation. (a) A snapshot of potential temperature at 340 m depth, showing the eddy stirring of modified Warm Deep Water (mWDW) onto the continental shelf beneath the Antarctic Slope Front (ASF). (b) A snapshot of depth-averaged vortex Rossby number (see Section 4), highlighting the presence of vortical structures along the continental slope, particularly to the west of Filchner Trough (FT). (c) Eddy-induced velocity $\boldsymbol{u}_{\text{eddy}}$, defined by (26), in the dense shelf water (DSW) layer. (d) Multi-annual mean depth-averaged eddy kinetic energy (EKE), defined in (25). (e,f) Depth-integrated rates of EKE production from (e) potential energy and (f) mean kinetic energy. The inset in panel (e) shows production of EKE from potential energy around the mouth of the Filchner Trough. Water column thickness in meters is shown in contours in panels (a–b) and (d–f), and in colors in panel (c).

baroclinic eddy generation associated with the FT overflow is the primary source of the eddies along the continental slope. Specifically, we compute the generation of EKE via conversion from potential energy (PE),

$$\text{PE} \rightarrow \text{EKE} \approx g \left\langle \tilde{\alpha}\, \overline{w'\theta'} - \tilde{\beta}\, \overline{w'S'} \right\rangle, \qquad (27)$$

and via conversion from mean kinetic energy (MKE),

$$\mathrm{MKE} \rightarrow \mathrm{EKE} = -\left\langle \overline{\boldsymbol{u}_h'\boldsymbol{u}'} \cdot \nabla \overline{\boldsymbol{u}_h} \right\rangle. \tag{28}$$

The PE → EKE conversion is elevated in the same locations as the EKE, particularly at the mouth of the FT, where it is approximately an order of magnitude larger than in other portions of the continental slope (note that the color scale is saturated around Filchner trough in Fig. 11(e)). In contrast the MKE → EKE conversion is typically an order of magnitude smaller than that of the PE → EKE conversion, and is negative (indicating descruction of EKE) in the FT overflow. Taken together, these diagnostics strongly suggest that the non-tidal, sub-monthly variability in our model simulations is largely comprised of baroclinically-generated eddies, primarily associated with dense overflows.

e. Sensitivity to model resolution and inclusion of tides

We now test the importance of both model horizontal resolution and the inclusion of tides by comparing various aspects of the Weddell Sea overturning circulation between our six simulations (see Section 2). Figs. 12(a–c) show the dependence of our metrics of the overturning circulation strength, $\Psi_{\max}$, the continental shelf overturning strength, Ψ_{shelf}, and the FRIS overturning Ψ_{FRIS}, to horizontal resolution and the inclusion of tides. In each case we plot both the strength of the time-mean overturning circulation, *e.g.* $\langle\Psi\rangle_{\max}$, and the time-mean overturning circulation strength, *e.g.* $\langle\Psi_{\max}\rangle$. The former is typically weaker because seasonal/interannual fluctuations in the isopycnal transports may cancel out when averaged over the full 8-year analysis period. Figs. 12(d) shows an analogous plot of the eddy-driven circulation across the shelf break,

$$\Psi_{\mathrm{eddy}}(t) = \max_{1.5<\eta<5.5,\,\sigma} \left\{ -\psi^{\sigma}_{\mathrm{eddy}} \right\}. \tag{29}$$

Both Ψ_{shelf} and Ψ_{FRIS} show modest sensitivities to the model resolution and to the inclusion of tides, which each produce changes of ∼0.2 Sv. However, $\Psi_{\max}$ increases by around 50% when the model resolution is coarsened to 1/3°. This is may be due to increased lateral mixing between the DSW overflow and ambient water masses on the model's z-coordinate vertical grid (Griffies et al. 2000). Increasing the horizontal resolution from 1/3° to 1/12° decreases Ψ_{eddy} by almost 50%, or an absolute decrease of 2 Sv, which is approximately equal to the decrease in $\Psi_{\max}$. Both $\Psi_{\max}$ and Ψ_{eddy} exhibit relatively little change in response to the inclusion of tides, consistent with our earlier inference that tides contribute little to the sub-monthly component of the overturning circulation.

In Fig. 12(e–f) we additionally quantify the impact of model resolution and the inclusion of tides on the density of the exported waters. We define the density of the outflowing dense waters via an integral weighted by the overturning streamfunction ψ^{σ},

$$\sigma_{\mathrm{outflow}}(\eta, \bar{t}) = \frac{\displaystyle\int_{\infty}^{\sigma_{\max}} \frac{\partial \psi^{\sigma}}{\partial \sigma}\, \sigma \,\mathrm{d}\sigma}{\displaystyle\int_{\infty}^{\sigma_{\max}} \frac{\partial \psi^{\sigma}}{\partial \sigma}\, \mathrm{d}\sigma}. \tag{30}$$

Here $\sigma_{\max}(\eta)$ denotes the density at which the streamfunction reaches its maximum amplitude, *i.e.* the transport is northward for densities greater than $\sigma_{\max}$. We quantify the density of the exported DSW via $\sigma_{\mathrm{DSW}} = \sigma_{\mathrm{outflow}}|_{\eta=3.5}$, close to the shelf break, and we quantify the density of newly formed WSDW via $\sigma_{\mathrm{WSDW}} = \sigma_{\mathrm{outflow}}|_{\eta=8}$, close to the northern boundary of the model domain. Fig. 12(e–f) shows that both σ_{WSDW} and σ_{DSW} are largely insensitive to model resolution and the inclusion of tides: the exported waters are ∼0.02–0.03 kg m^{-3} lighter at the highest (1/12°) resolution, and lighten by only ∼0.01–0.02 kg m^{-3} when tides are included. Hausmann et al. (2020) similarly reported a slight freshening and lightening of the densest waters exported from the continental shelf in response to the inclusion of tides. The tidally-induced lightening of the exported waters is related to the melt rate of the FRIS, which increases by ∼30% when tides are included (Fig. 12(g)). However, the impact of this increased melt on the total buoyancy loss over the continental shelf ($\eta < 4$) is relatively small (Fig. 12(h)), which explains the modest impact on the overturning strength and the density of the exported waters.

5. Discussion and conclusions

Previous studies have shown that overturning on the Antarctic continental shelf may be influenced by a range of different processes, including tidal flows, various forms of mesoscale variability, and seasonal/interannual wind and buoyancy forcing (*e.g.* Thompson et al. 2018; Stewart et al. 2019). However, the relative importance of these processes for water mass transports and transformations has not previously been quantified. In this study we used a high-resolution regional model (see Section 2) to investigate their contributions to driving the overturning circulation in the Weddell Sea. This is a key site in the near Antarctic overturning circulation, being responsible for approximately 8 Sv of the 10–20 Sv total AABW production (Jullion et al. 2014; Vernet et al. 2019).

Our primary analysis tools are streamfunctions computed in quasi-latitude/density space (Döös and Webb 1994; Wolfe 2014) and in temperature/salinity space (Zika et al. 2012; Döös et al. 2012). These streamfunctions directly quantify water mass transports and water mass transformations, respectively, and thus offer complementary perspectives on the Weddell Sea overturning circulation. While these streamfunctions provide consistent quantifications of the overturning circulation (compare Figs. 4

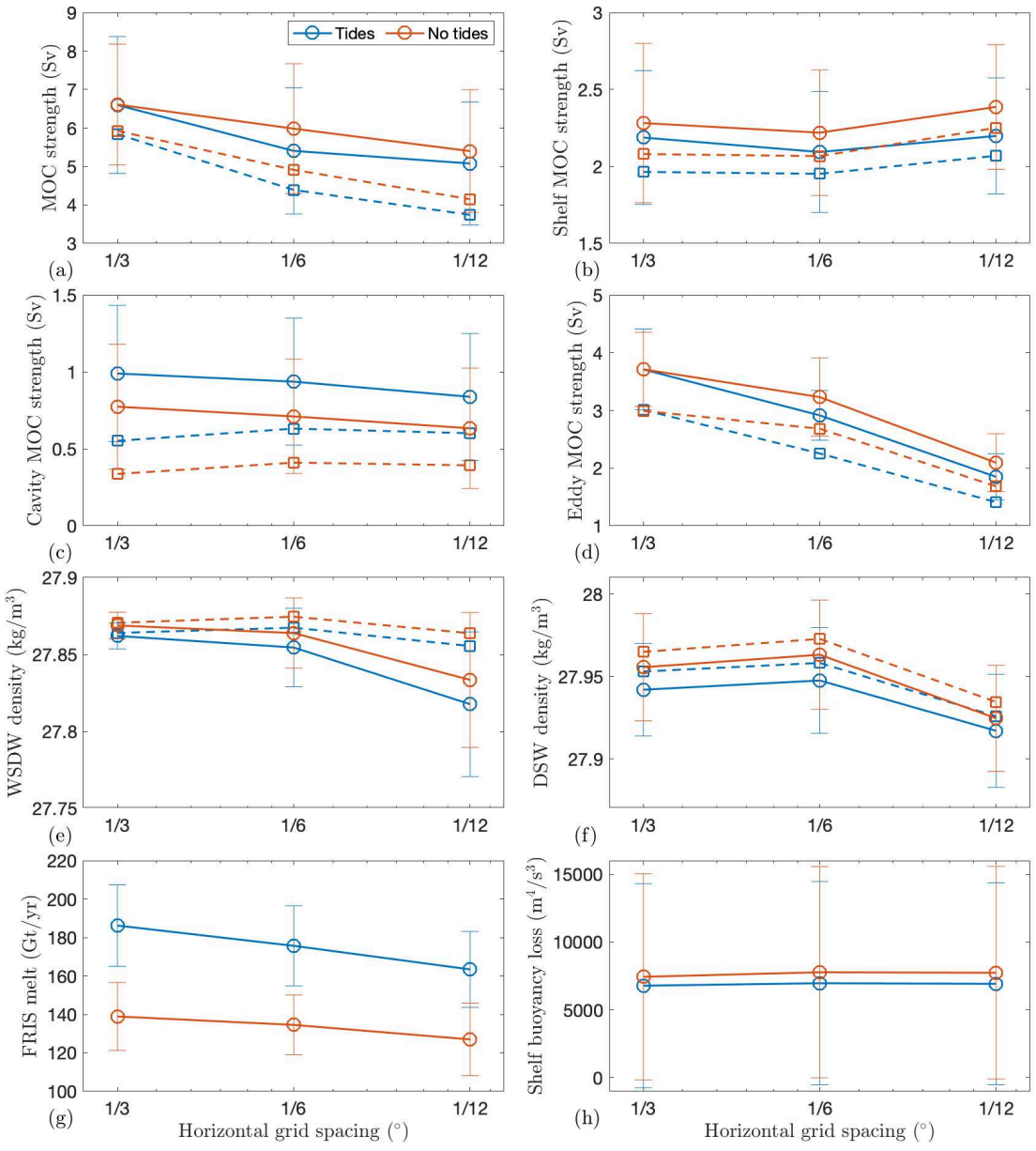

FIG. 12. Sensitivity of various overturning circulation metrics to model horizontal grid spacing and the inclusion of tides, defined in Section 4. (a) Weddell Sea overturning strength $\Psi_{\max}$, (b) continental shelf overturning strength Ψ_{shelf}, (c) Filchner Ronne Ice Shelf cavity overturning strength Ψ_{FRIS}, (d) shelf break eddy overturning strength Ψ_{eddy}, (e) density of exported Weddell Sea Deep Water (WSDW), σ_{WSDW}, (f) density of exported dense shelf waters (DSW), σ_{DSW}, (g) total melt rate of the FRIS, (h) total buoyancy loss on the southern Weddell Sea continental shelf. In (a–h) we plot the mean of each metric over all months in the 8-year analysis period and its standard deviation, *e.g.* $\langle\Psi_{\max}\rangle$ and std($\Psi_{\max}$), using solid lines with circular symbols and one standard deviation error bars. In (a–f) we additionally plot each metric as computed using the multi-annual mean fields, *e.g.* $\langle\Psi\rangle_{\max}$, using dashed lines and square symbols.

and 5), both produce an artificial localized overturning circulation in the FRIS cavity. We offer a possible approach to reconciling the overturning streamfunction with the pathways of DSW via a horizontal coordinate transformation in Appendix C.

The simulated strength, pathways and variability of the simulated overturning circulation agree qualitatively and quantitatively with established understanding of this region based on previous studies (Section 3). Specifically, the model simulates approximately 1.75 Sv of transforma-

tion from Winter Waters to High Salinity Shelf Waters and Ice Shelf Water on the southern Weddell Sea continental shelf (Figs. 4–5), comparable to observational estimates (Foldvik et al. 2004). These simulated dense shelf waters (DSW) are routed through the FRIS cavity and the Filchner Trough (Fig. 6), before overflowing and descending the continental slope as they flow westward around the Weddell Gyre. Entrainment of overlying waters lightens the exported waters and increases the net simulated volume flux to 4 Sv by the time they reach the northern edge of the regional model domain, also consistent with observational estimates (Foldvik et al. 2004). The simulated overturning circulation exhibits substantial seasonal and interannual variability in the open Weddell gyre and in the FRIS cavity, but relatively weak variability over the continental shelf (Fig. 7).

In Section 4 we decomposed the simulated overturning circulation and the associated fluxes of heat and salt into contributions attributable to multi-annual mean flows, seasonal/interannual fluctuations, tides, and other sub-monthly variability. Counter to our expectations based on previous studies (*e.g.* Padman et al. 2009; Wang et al. 2013), tides do not drive a substantial rectified transport of water masses (Section 4). The most pronounced impact of tides is in the FRIS cavity, where they increase the melt rate and cavity overturning strength by ∼30%, but these changes only reduce the export of dense waters by less than 10% (Fig. 12). Seasonal/interannual fluctuations also contribute modestly to the net simulated overturning circulation, as discussed in Section 4. Our examination of the energy budget indicates that the non-tidal sub-monthly variability is primarily comprised of baroclinically-generated eddies associated with dense overflows, though we cannot exclude other contributions, *e.g.* from high-frequency wind-driven variability. These eddies are of comparable importance to the mean flow in exporting the simulated DSW across the Weddell Sea continental shelf break (Fig. 8). These eddies also play a significant role in the transfer of water parcels between WDW, WW, and HSSW (Fig. 9), though it should be noted that this quantification of the eddy-driven water transformations is an estimate derived via the NTRM (see Section 3). Furthermore, eddies account for 100% of the simulated shoreward transport of heat across the continental shelf break, via a combination of eddy advection and eddy isopycnal stirring (Fig. 10). This is consistent with previous studies that have shown that export of DSW pumps momentum upward into overlying, warmer waters and drives shoreward transport (Stewart and Thompson 2016; Morrison et al. 2020). The modeled eddy activity is concentrated along the southern Weddell Sea continental slope, particlarly around Filchner Trough, and is sourced from baroclinic energy conversion in the overflowing DSW (Fig. 11). This is consistent with the findings of previous studies using laboratory and numerical experiments (Baines and Condie 1998; Wang et al. 2009; Stewart and Thompson 2016).

A caveat of our modeling approach is that although the model's horizontal grid spacing of 1/12°, or ∼2 km along the front of the FRIS, demonstrably permits eddies (Fig. 11), even finer resolution may be required to fully resolve the eddy field (St-Laurent et al. 2013; Stewart and Thompson 2015a). It is unclear whether finer resolution would further suppress the eddy-driven overturning, as is the trend in Fig. 12, or enhance it via improved resolution of baroclinic instability in the overflow. A similar caveat applies to the representation of the tides: finer resolution of the baroclinic flows induced by the tidal forcing could potentially produce a rectified cross-slope transport of water masses, as suggested by previous studies (Padman et al. 2009; Wang et al. 2013). The strength of the overturning circulation is largely captured in our coarser (1/3° and 1/6°) simulations (see Fig. 12). However, the eddy-driven component is strongly sensitive to horizontal resolution, decreasing in magnitude by a factor of 2 as the grid spacing is refined from 1/3° to 1/12°. This weakening as the horizontal grid increasingly resolves the first Rossby radius of deformation contrasts with previous idealized modeling results (Stewart and Thompson 2015a) and expectations based on linear theories of baroclinic instability (Vallis 2017). The dynamical reasons underlying this finding remain to be explored in future work.

The influence of variability on interannual and longer time scales is likely under-represented in our model due to the relatively short (8-year) duration of the analysis period. DSW production has been shown to have decreased and then recovered on decadal time scales, in both the Ross Sea (Silvano et al. 2020) and the Weddell Sea (Abrahamsen et al. 2019), which would undoubtedly have a rectified effect on the multi-decadal-averaged overturning circulation. Interannual/decadal variability may also result from the opening of the Weddell polynya, which also indirectly modifies shelf water properties (Dufour et al. 2017; Naughten et al. 2019), or due to long-term trends in the Antarctic atmospheric circulation and glacial melt (Spence et al. 2014; Hazel and Stewart 2019; Morrison et al. 2020). Interannual variability is further suppressed in our model configuration by the open boundary conditions, which only vary seasonally. Interannual or decadal upstream changes in the salinity of Eastern Slope Waters or in the depth of the pycnocline may be expected to translate to changes in the salinity of HSSW and potentially to the melt rate of the FRIS (Graham et al. 2013; Daae et al. 2017).

Finally, we note that the decomposition of the drivers of the Weddell Sea overturning presented in this study is both inexact and incomplete, as is the simulated overturning circulation itself. Our separation of the variability into sub-monthly and seasonal/interannual variability is arbitrary, yet it appears to distinguish qualitatively different contributions to the overturning circulation (Figs. 8–9). How-

ever, we cannot exclude the possibility that, *e.g.*, mesoscale variability is contributing to the seasonal/interannual component of the overturning, or that the seasonal cycle is contributing to the sub-monthly component of the overturning. There remains a spectrum of oceanic flows at length scales too small to be represented explicitly in this model, which might yet conceivably contribute to driving the MOC. In particular, submesoscale motions, particularly around the coastal polynyas at the ice shelf front, might be important for surmounting the potential vorticity gradient imposed by the ice shelf face (Årthun et al. 2013; Li et al. 2017; Wåhlin et al. 2020). Submesoscale motions, in particular symmetric instabilities, may also manifest in the overflows of DSW (Yankovsky and Legg 2019) or in the outflow of ISW from the FRIS cavity (Naveira Garabato et al. 2017). Internal wave motions, particularly those generated by the tides, also likely develop three-dimensional patterns of water mass transformation that shape the MOC, *e.g.* by deepening the bottom boundary layer over the continental slope (Fer et al. 2016; Daae et al. 2019). Due to the practical limitations of directly observing such phenomena, further refinements of regional and process-oriented models likely offer the most promising near-term approach to addressing their role in the near-Antarctic overturning circulation.

Acknowledgments. The author acknowledges Julia Hazel's assistance with the configuration of the regional model used in this study. This material is based in part upon work supported by the National Science Foundation under Grant Numbers OPP-1543388 and OCE-1751386, and by the National Aeronautics and Space Administration ROSES Physical Oceanography program under grant number 80NSSC19K1192. This work used the Extreme Science and Engineering Discovery Environment (XSEDE, Towns et al. 2014), which is supported by National Science Foundation grant number ACI-1548562. The authors thank Ralph Timmermann and two anonymous reviewers for many constructive comments that improved the submitted manuscript.

Data availability statement. All new data presented in this study are output from model simulations using the publicly-available Massachusetts Institute of Technology general circulation model (MITgcm), which is available via `http://mitgcm.org/`. Matlab scripts used to generate, run, and analyze these simulations are available via `https://doi.org/10.5281/zenodo.4397076`. The simulation output files are available via `https://doi.org/10.15144/S41595`.

APPENDIX A

Overturning in Neutral Density coordinates

As noted in Section 3, using surface-referenced potential density as a vertical coordinate in our overturning circulation calculations might introduce distortions: in the Weddell Sea the slopes of potential density surfaces may differ substantially from the slopes of neutral surfaces (McDougall 1987), and potential density is typically vertically non-monotonic in this region, regardless of the reference level (Stewart and Thompson 2015b). Various previous studies have used neutral surfaces (Nicholls et al. 2009) or the Neutral Density variable of Jackett and McDougall (1997) to circumvent this issue (*e.g.* Thompson and Heywood 2008; Chavanne et al. 2010; Jullion et al. 2014). Here we show that computing the overturning circulation in Neutral Density surfaces yields an almost identical overturning streamfunction in quasi-latitude/density space. We note that there are various alternative approaches to constructing approximately neutral surfaces (*e.g.* de Szoeke et al. 2000; Klocker et al. 2009; Stanley 2019; Lang et al. 2020); our aim here is not to achieve an optimal representation of isopycnal fluxes in the Weddell Sea, but rather to test whether our use of potential density is distorting the computed overturning circulation.

The Neutral Density variable of (Jackett and McDougall 1997), which we denote as γ^{JM97}, is not defined in a substantial fraction of the FRIS cavity. We therefore compute a new three-dimensional Neutral Density reference climatology based on the model's mean state, which we denote as γ^{ref}. Our approach follows that of Stewart (2019), to which the reader is referred for algorithmic details. Briefly, we first set $\gamma^{\mathrm{ref}} = \gamma^{\mathrm{JM97}}$ in the northeasternmost column of grid cells in our model domain, where γ^{JM97} is computed from the multi-annual mean $\langle\overline{S}\rangle$ and $\langle\overline{\theta}\rangle$. This ensures that γ^{ref} remains close to γ^{JM97} throughout the model domain. We then iteratively label each model grid cell n with a γ^{ref} value, moving from the northeastern to the southwestern corner, by referring the time-mean properties in that grid cell $(\langle\overline{S_n}\rangle, \langle\overline{\theta_n}\rangle, z_n)$ to already-assigned water columns via the discrete neutral relation (Jackett and McDougall 1997; Stewart and Thompson 2015b).

In Fig. A13(a) we plot a section of γ^{ref} along 38°W. In the upper ocean the isopycnal structures are very similar to those shown in Fig. 4(b), as expected, though there are visible differences in the isopycnal slopes in the deep ocean. Fig. A13(b) compares the vertical stratification of γ^{ref}, which we denote as N^2_{ref} with the true buoyancy frequency N^2 from (11). Although there is necessarily a difference between the stratification of any approximate Neutral Density variable and the buoyancy frequency (Eden and Willebrand 1999), in general the buoyancy N^2_{ref} is consistently around twice the true buoyancy frequency N^2. This factor of two is inherited from the "b-factor" of Jackett and McDougall (1997), which they set to $b = 2$ in this region. In Fig. A13(c) we compare γ^{ref} with surface-referenced potential density σ, and show that they covary closely throughout the model domain. Thus despite some apparent differences in the isopycnal slopes in Figs. 4(b) and A13(a), we anticipate that volume fluxes in γ^{ref} and σ

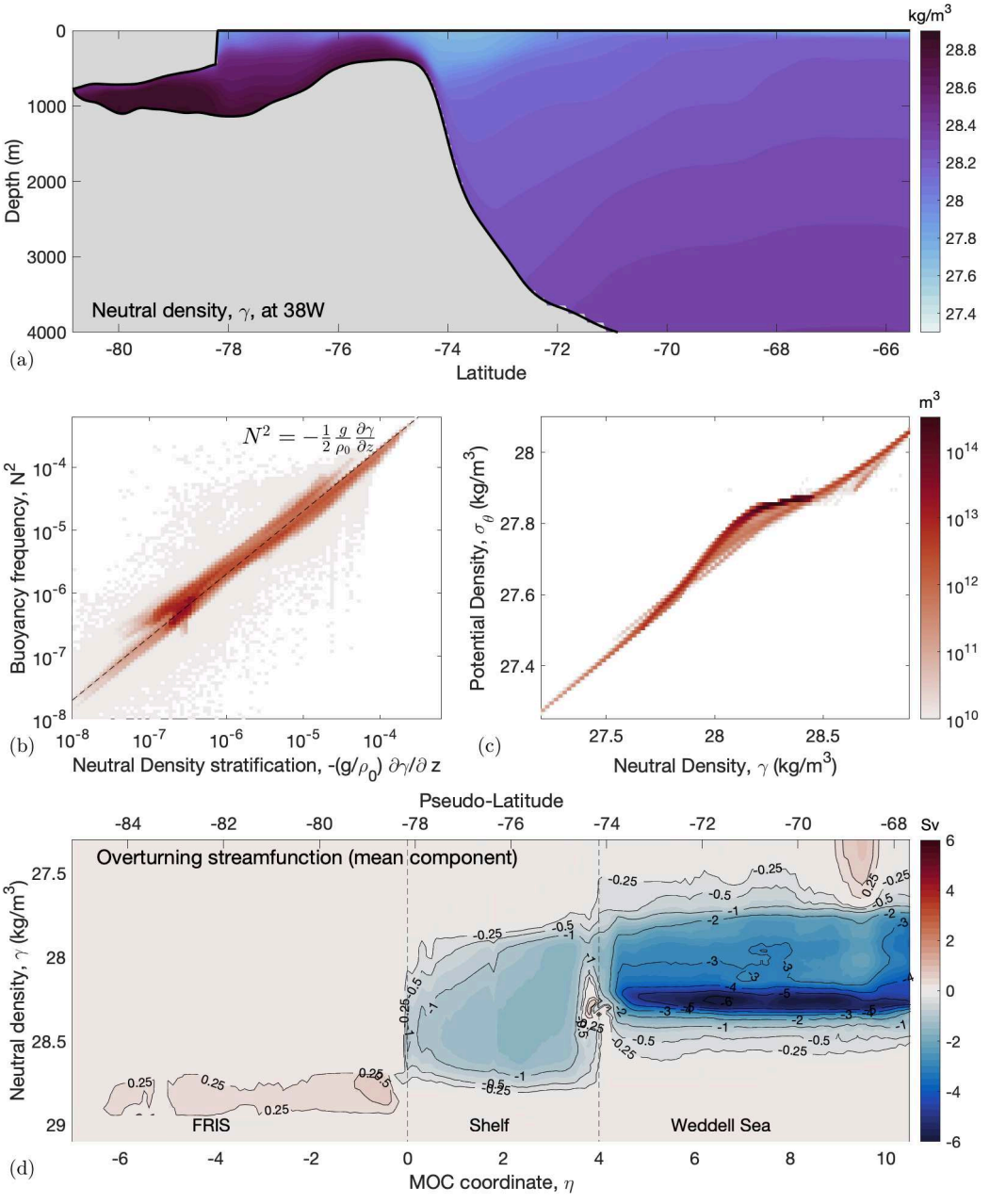

FIG. A13. Weddell Sea overturning in Neutral Density space (see Appendix A). (a) As Fig. 4(b) but instead showing a section of our reference Neutral Density variable γ^{ref}, derived from the model's multi-annual mean thermodynamic state in our TIDES6 simulation. (b) Relationship between the vertical stratification of γ^{ref} and the time-mean buoyancy frequency N^2. Colors indicate the volume of the model domain contained in each bin of logarithmic size 0.05×0.05. (c) Relationship between γ^{ref} and surface-referenced potential density σ^{θ}. Colors indicate the volume of the model domain contained in each bin of logarithmic size $0.01 \times 0.01\,\text{kg}\,\text{m}^{-3}$. (d) Mean component of the overturning circulation in Neutral Density (Jackett and McDougall 1997) space, $\psi^{\gamma}_{\text{mean}}$ (see Section 4).

surfaces should not differ substantially. To test this, in Fig. A13(d) we compute the multi-annual mean component of the density overturning streamfunction, which we denote $\psi^{\gamma}_{\text{mean}}$ in analogy with (17). We performed this calculation using output from our TIDES6 simulation, rather than NOTIDES12, due to the computational cost of computing $\psi^{\gamma}_{\text{ref}}$ at higher resolution. While a direct quantitative comparison can therefore not be made between Figs. 8(a)

and A13(d), the results are in fact both qualitatively and quantitatively similar. We therefore conclude that our use of σ to compute isopycnal fluxes has not substantially distorted the presentation of the overturning circulation ψ^{σ}, and that an approximate estimate of the fluxes in Neutral Density surfaces could be achieved by remapping σ to γ^{ref} via the relationship shown in Fig. A13(c).

APPENDIX B

Evaluation of Neutral Temporal Residual Mean volume fluxes

In Section 3 we constructed the thermohaline overturning circulation by combining the monthly-mean flow $\overline{\boldsymbol{u}}$ with an eddy-induced transport velocity $\boldsymbol{u}^{\star}$, consistent with previous studies (Zika et al. 2012; Döös et al. 2012). However, whereas we were able to compute the "eddy" component of the volume fluxes in density space directly from the model output (see Section 4), in thermohaline coordinates we estimated $\boldsymbol{u}^{\star}$ via the Neutral Temporal Residual Mean (Stewart 2019). In Fig. B14 we evaluate the accuracy of the eddy-induced transport $\boldsymbol{u}^{\star}$ by comparing the eddy streamfunction in (17) with a streamfunction derived from fluxes due to $\boldsymbol{u}^{\star}$ in σ-layers,

$$\boldsymbol{U}_{\text{NTRM}}(x, y, \sigma, \bar{t}) = \int_{z_{\text{bot}}}^{\overline{\sigma'}=\sigma} \boldsymbol{u}_h^{\star}\, \mathrm{d}z. \tag{B1}$$

There are some visible differences between the diagnosed eddy streamfunction and the NTRM streamfunction. In particular, there is a relatively weak (~0.5 Sv) positive eddy-driven overturning offshore $5 \lesssim \eta \lesssim 6$ that is absent in the NTRM streamfunction. However the NTRM does quantitatively capture the eddy-driven export of dense water across the southern Weddell Sea continental shelf: the NTRM slightly underestimates the magnitude of this transport by 10–20%. It is therefore likely that Fig. 9(c) slightly underestimates the strength of the eddy-induced overturning in θ–S space, and therefore that Fig. 5(c) slightly underestimates the strength of the net thermohaline circulation.

APPENDIX C

An alternative "MOC coordinate" for the FRIS cavity

Figs. 4 and 5 both exhibit a distinct overturning cell in the FRIS cavity, with dense HSSW flowing in and lighter ISW flowing out. While the strength of this cell provides a useful quantification of the circulation within the FRIS cavity, Fig. 6 suggests that its presence is somewhat artificial: much of the newly formed dense water circulates through the cavity before overflowing at the mouth of the Filchner Trough (see Nicholls et al. 2009). This suggests that the apparent separation of the FRIS overturning cell in Figs. 4 and 5 is somewhat artificial, and results from water masses crossing the same portion of (η, σ) and (S, θ) space in different physical locations, which cancel out when collapsed into a two-dimensional visualization of the overturning (see Nurser and Lee 2004).

One way to remove the artificial separation of the FRIS overturning cell is to select an alternative coordinate system. Fig. C15(a) shows an example of such a coordinate system, in which the MOC coordinate $\tilde{\eta}$ is exactly equal to η for $\eta = 4$, but in which iso-$\tilde{\eta}$ contours tend to circles surrounding the Ronne polynya as $\tilde{\eta} \to 0$. Fig. C15(b) shows the overturning circulation computed in this modified MOC coordinate, *i.e.* $\langle \psi^{\sigma} \rangle (\tilde{\eta}, \sigma)$. In this coordinate system the very densest water is formed at $\tilde{\eta} = 0$, in the Ronne polynya. This water lightens as it flows from $\tilde{\eta} = 0$ to $\tilde{\eta} = 2$, likely due to the input of freshwater from melting of the FRIS. The density of the northward-flowing water then remains approximately unchanged until $\tilde{\eta} \approx 4$, where it overflows and entrains lighter waters, as in Fig. 4(c). Note that the overturning streamfunction in the modified coordinate system would yield almost identical estimates of the overturning strength over the continental shelf and in the open ocean, as the overturning strengthens with distance from the FRIS. We therefore chose to present the overturning circulation in (η, σ) rather than $(\tilde{\eta}, \sigma)$ coordinates in the main text, as the interpretation of η is simpler, and because the former also offers an estimate of the cavity circulation strength.

References

Abrahamsen, E. P., and Coauthors, 2019: Stabilization of dense Antarctic water supply to the Atlantic Ocean overturning circulation. *Nat. Clim. Change*, **9 (10)**, 742–746.

Adkins, J. F., 2013: The role of deep ocean circulation in setting glacial climates. *Paleoceanography*, **28 (3)**, 539–561.

Årthun, M., P. R. Holland, K. W. Nicholls, and D. L. Feltham, 2013: Eddy-driven exchange between the open ocean and a sub–ice shelf cavity. *J. Phys. Oceanogr.*, **43 (11)**, 2372–2387.

Baines, P. G., and S. Condie, 1998: Observations and modelling of Antarctic downslope flows: A review. *Ocean, Ice, and Atmosphere: Interactions at the Antarctic Continental Margin, Antarct. Res. Ser*, **75**, 29–49.

Carmack, E. C., and T. D. Foster, 1975: On the flow of water out of the Weddell Sea. *Deep Sea Res.*, Elsevier, Vol. 22, 711–724.

Chavanne, C. P., K. J. Heywood, K. W. Nicholls, and I. Fer, 2010: Observations of the Antarctic slope undercurrent in the southeastern Weddell Sea. *Geophys. Res. Lett.*, **37 (13)**.

Daae, K., E. Darelius, I. Fer, S. Østerhus, and S. Ryan, 2018: Wind stress mediated variability of the Filchner Trough overflow, Weddell Sea. *J. Geophys. Res. Oceans*, **123 (5)**, 3186–3203.

Daae, K., I. Fer, and E. Darelius, 2019: Variability and mixing of the Filchner overflow plume on the continental slope, Weddell Sea. *J. Phys. Oceanogr.*, **49 (1)**, 3–20.

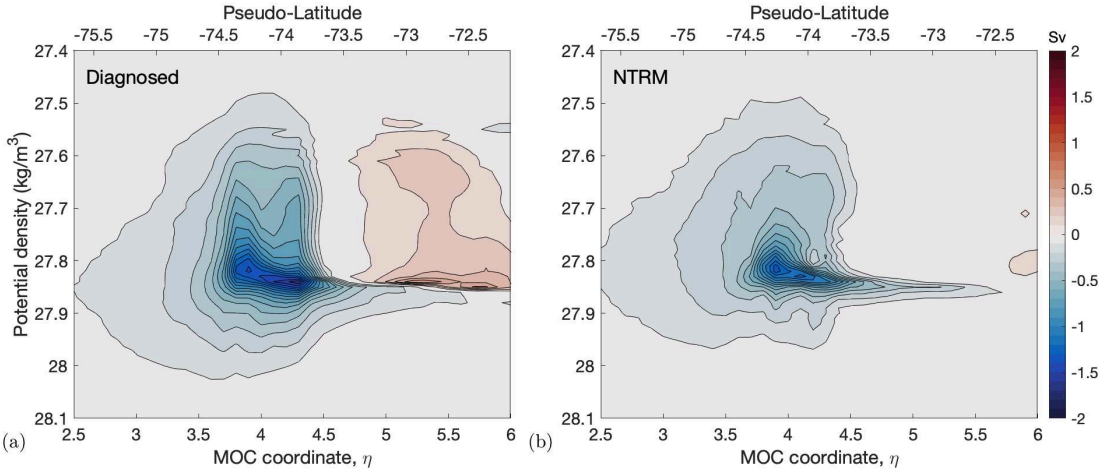

FIG. B14. Evaluation of eddy fluxes approximated via the Neutral Temporal Residual Mean (NTRM; see Appendix B). (a) As Fig. 8(c) except showing the eddy overturning $\langle \psi^{\sigma}_{\text{eddy}} \rangle$ only in the vicinty of the shelf break $\eta \approx 4$. (b) As panel (a), but with isopycnal fluxes computed using the NTRM via (B1).

Daae, K., T. Hattermann, E. Darelius, and I. Fer, 2017: On the effect of topography and wind on warm water inflow: An idealized study of the southern Weddell Sea continental shelf system. *Journal of Geophysical Research: Oceans*.

Darelius, E., I. Fer, and K. W. Nicholls, 2016: Observed vulnerability of Filchner-Ronne Ice Shelf to wind-driven inflow of warm deep water. *Nature communications*, **7**, 12 300.

Darelius, E., K. Makinson, K. Daae, I. Fer, P. R. Holland, and K. W. Nicholls, 2014: Hydrography and circulation in the Filchner depression, Weddell Sea, Antarctica. *J. Geophys. Res. Oceans*, **119 (9)**, 5797–5814.

Darelius, E., and J.-B. Sallee, 2018: Seasonal outflow of ice shelf water across the front of the Filchner ice shelf, Weddell Sea, Antarctica. *Geophysical Research Letters*, **45 (8)**, 3577–3585.

Darelius, E., L. Smedsrud, S. Østerhus, A. Foldvik, and T. Gammelsrød, 2009: Structure and variability of the Filchner overflow plume. *Tellus A: Dynamic Meteorology and Oceanography*, **61 (3)**, 446–464.

de Szoeke, R. A., S. R. Springer, and D. M. Oxilia, 2000: Orthobaric density: A thermodynamic variable for ocean circulation studies. *J. Phys. Oceanogr.*, **30 (11)**, 2830–2852.

Dinniman, M. S., X. S. Asay-Davis, B. K. Galton-Fenzi, P. R. Holland, A. Jenkins, and R. Timmermann, 2016: Modeling ice shelf/ocean interaction in Antarctica: A review. *Oceanography*, **29 (4)**, 144–153.

Döös, K., J. Nilsson, J. Nycander, L. Brodeau, and M. Ballarotta, 2012: The world ocean thermohaline circulation. *J. Phys. Oceanogr.*, **42 (9)**, 1445–1460.

Döös, K., and D. J. Webb, 1994: The Deacon cell and the other meridional cells of the Southern Ocean. *J. Phys. Oceanogr.*, **24 (2)**, 429–442.

Dufour, C. O., A. K. Morrison, S. M. Griffies, I. Frenger, H. Zanowski, and M. Winton, 2017: Preconditioning of the Weddell Sea polynya by the ocean mesoscale and dense water overflows. *J. Climate*, **30 (19)**, 7719–7737.

Eden, C., and J. Willebrand, 1999: Neutral density revisited. *Deep Sea Res. Pt. II*, **46 (1-2)**, 33–54.

Fahrbach, E., R. G. Peterson, G. Rohardt, P. Schlosser, and R. Bayer, 1994: Suppression of bottom water formation in the southeastern Weddell Sea. *Deep Sea Res. Pt. I*, **41 (2)**, 389–411.

Fer, I., E. Darelius, and K. B. Daae, 2016: Observations of energetic turbulence on the Weddell Sea continental slope. *Geophys. Res. Lett.*, **43 (2)**, 760–766.

Foldvik, A., and T. Gammelsrød, 1988: Notes on Southern Ocean hydrography, sea-ice and bottom water formation. *Palaeogeogr., Palaeoclimatol., Palaeoecol.*, **67 (1-2)**, 3–17.

Foldvik, A., T. Gammelsrød, S. Østerhus, E. Fahrbach, G. Rohardt, M. Schröder, L. Nicholls, K. W. Padman, and R. Woodgate, 2004: Ice shelf water overflow and bottom water formation in the southern Weddell Sea. *Journal of Geophysical Research: Oceans*, **109 (C2)**.

Foster, T. D., and E. C. Carmack, 1976: Frontal zone mixing and Antarctic Bottom Water formation in the southern Weddell Sea. *Deep Sea Res.*, Elsevier, Vol. 23, 301–317.

Gent, P. R., and J. C. McWilliams, 1990: Isopycnal mixing in ocean circulation models. *J. Phys. Oceanogr.*, **20 (1)**, 150–155.

Graham, J. A., K. J. Heywood, C. P. Chavanne, and P. R. Holland, 2013: Seasonal variability of water masses and transport on the Antarctic continental shelf and slope in the southeastern Weddell Sea. *Journal of Geophysical Research: Oceans*, **118 (4)**, 2201–2214.

Griffies, S. M., R. C. Pacanowski, and R. W. Hallberg, 2000: Spurious diapycnal mixing associated with advection in a z-coordinate ocean model. *Mon. Weather Rev.*, **128 (3)**, 538–564.

Groeskamp, S., S. M. Griffies, D. Iudicone, R. Marsh, A. J. G. Nurser, and J. D. Zika, 2019: The water mass transformation framework for ocean physics and biogeochemistry. *Ann. Rev. Mar. Sci.*, **11**, 271–305.

Grosfeld, K., and R. Gerdes, 1998: Circulation beneath the Filchner Ice Shelf, Antarctica, and its sensitivity to changes in the oceanic environment: a case-study. *Ann. Glaciol.*, **27**, 99–104.

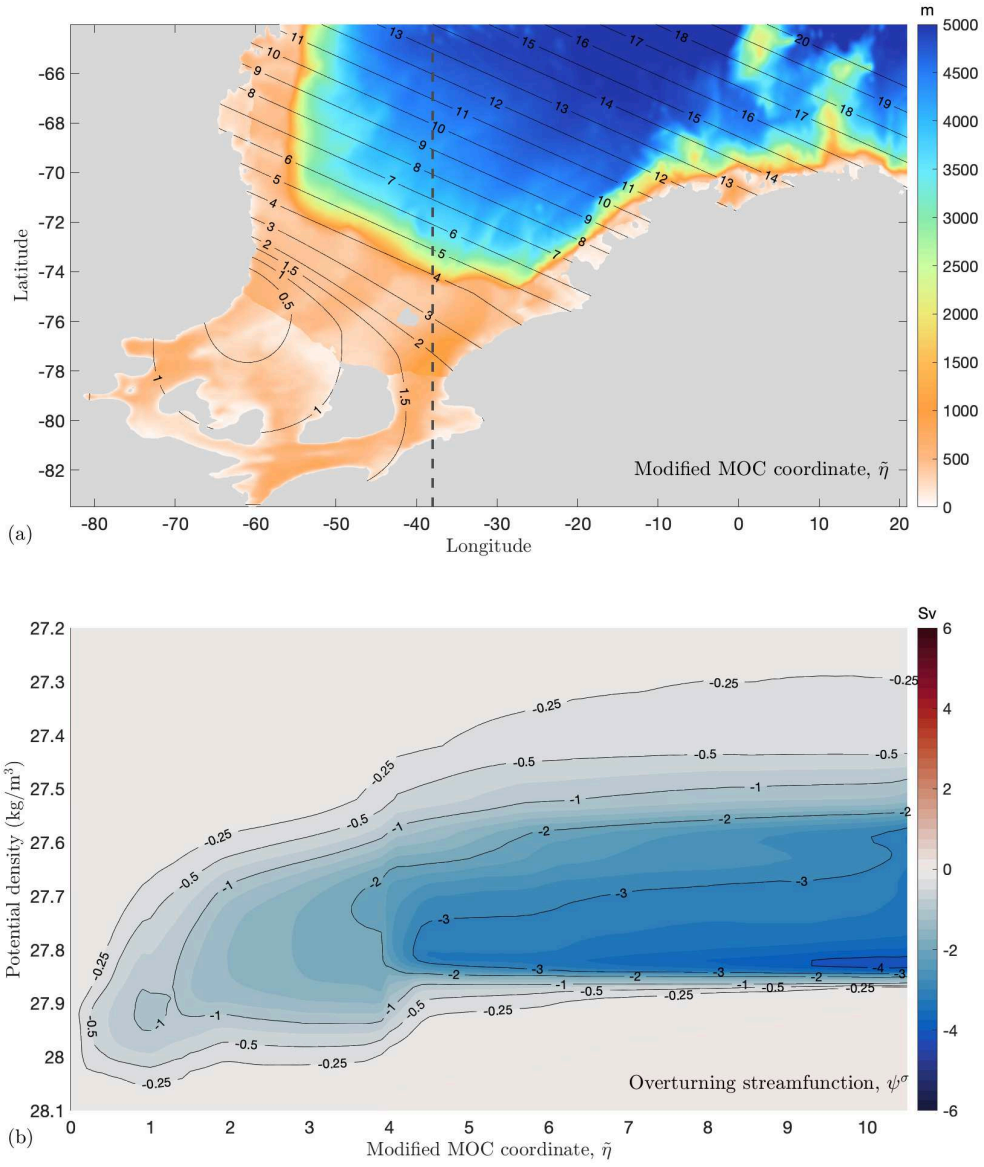

FIG. C15. As Fig. 4(a,c), but using a modified MOC coordinate $\tilde{\eta}$ that approaches zero in the Ronne polynya (see Appendix C).

Haid, V., and R. Timmermann, 2013: Simulated heat flux and sea ice production at coastal polynyas in the southwestern Weddell Sea. *Journal of Geophysical Research: Oceans*, **118 (5)**, 2640–2652.

Hausmann, U., J.-B. Sallée, N. C. Jourdain, P. Mathiot, C. Rousset, G. Madec, J. Deshayes, and T. Hattermann, 2020: The role of tides in ocean–ice-shelf interactions in the southwestern Weddell Sea. *J. Geophys. Res. Oceans*, e2019JC015847.

Hazel, J. E., and A. L. Stewart, 2019: Are the Near-Antarctic Easterly Winds Weakening in Response to Enhancement of the Southern Annular Mode? *Journal of Climate*, **32 (6)**, 1895–1918.

Hazel, J. E., and A. L. Stewart, 2020: Bistability of the Filchner-Ronne Ice Shelf Cavity Circulation and Basal Melt. *J. Geophys. Res.*, **125 (4)**, e2019JC015 848.

Hellmer, H. H., and A. Beckmann, 2001: The Southern Ocean: A ventilation contributor with multiple sources. *Geophys. Res. Lett.*, **28 (15)**, 2927–2930.

Hibler III, W. D., 1979: A dynamic thermodynamic sea ice model. *Journal of Physical Oceanography*, **9 (4)**, 815–846.

Hogg, A. M., P. Spence, O. A. Saenko, and S. M. Downes, 2017: The energetics of Southern Ocean upwelling. *J. Phys. Oceanogr.*, **47 (1)**, 135–153.

Huber, B., 2010: Physical oceanography during ICEFLOW cruise IC92. PANGAEA, URL https://doi.org/10.1594/PANGAEA.742743, doi: 10.1594/PANGAEA.742743.

Jackett, D. R., and T. J. Mcdougall, 1995: Minimal adjustment of hydrographic profiles to achieve static stability. *Journal of Atmospheric and Oceanic Technology*, **12 (2)**, 381–389.

Jackett, D. R., and T. J. McDougall, 1997: A neutral density variable for the world's oceans. *J. Phys. Oceanogr.*, **27 (2)**, 237–263.

Jacobs, S. S., 2004: Bottom water production and its links with the thermohaline circulation. *Antarct. Sci.*, **16 (4)**, 427.

Johnson, G. C., 2008: Quantifying Antarctic bottom water and North Atlantic deep water volumes. *J. Geophys. Res. Oceans*, **113 (C5)**.

Jourdain, N. C., P. Mathiot, N. Merino, G. Durand, J. Le Sommer, P. Spence, P. Dutrieux, and G. Madec, 2017: Ocean circulation and sea-ice thinning induced by melting ice shelves in the Amundsen Sea. *J. Geophys. Res. Oceans*, **122 (3)**, 2550–2573.

Jullion, L., and Coauthors, 2014: The contribution of the Weddell Gyre to the lower limb of the Global Overturning Circulation. *J. Geophys. Res. Oceans*, **119 (6)**, 3357–3377.

Klocker, A., T. J. McDougall, and D. R. Jackett, 2009: A new method for forming approximately neutral surfaces. *Ocean Sci. Discuss.*, **6 (2)**.

Lang, Y., G. J. Stanley, T. J. McDougall, and P. M. Barker, 2020: A pressure-invariant Neutral Density variable for the World's Oceans. *J. Phys. Oceanogr.*, **50 (12)**, 3585–3604.

Large, W. G., J. C. McWilliams, and S. C. Doney, 1994: Oceanic vertical mixing: A review and a model with a nonlocal boundary layer parameterization. *Reviews of Geophysics*, **32 (4)**, 363–403.

Legg, S., R. W. Hallberg, and J. B. Girton, 2006: Comparison of entrainment in overflows simulated by z-coordinate, isopycnal and nonhydrostatic models. *Ocean Modell.*, **11 (1-2)**, 69–97.

Li, Y., D. J. McGillicuddy Jr, M. S. Dinniman, and J. M. Klinck, 2017: Processes influencing formation of low-salinity high-biomass lenses near the edge of the Ross Ice Shelf. *J. Mar. Sys.*, **166**, 108–119.

Losch, M., 2008: Modeling ice shelf cavities in a z coordinate ocean general circulation model. *Journal of Geophysical Research: Oceans*, **113 (C8)**.

Losch, M., D. Menemenlis, J.-M. Campin, P. Heimbach, and C. Hill, 2010: On the formulation of sea-ice models. Part 1: Effects of different solver implementations and parameterizations. *Ocean Modell.*, **33 (1-2)**, 129–144.

Lumpkin, R., and K. Speer, 2007: Global ocean meridional overturning. *J. Phys. Oceanogr.*, **37 (10)**, 2550–2562.

Makinson, K., and K. W. Nicholls, 1999: Modeling tidal currents beneath Filchner–Ronne Ice Shelf and on the adjacent continental shelf: Their effect on mixing and transport. *J. Geophys. Res. Oceans*, **104 (C6)**, 13 449–13 465.

Malyarenko, A., A. J. Wells, P. J. Langhorne, N. J. Robinson, M. J. M. Williams, and K. W. Nicholls, 2020: A synthesis of thermodynamic ablation at ice-ocean interfaces from theory, observations and models. *Ocean Modell.*, 101692.

Marques, G. M., K. Padman, S. R. Springer, S. L. Howard, and T. M. Özgökmen, 2014: Topographic vorticity waves forced by Antarctic dense shelf water outflows. *Geophys. Res. Lett.*, **41 (4)**, 1247–1254.

Marshall, J., A. Adcroft, C. Hill, L. Perelman, and C. Heisey, 1997a: A finite-volume, incompressible Navier Stokes model for studies of the ocean on parallel computers. *Journal of Geophysical Research: Oceans*, **102 (C3)**, 5753–5766.

Marshall, J., C. Hill, L. Perelman, and A. Adcroft, 1997b: Hydrostatic, quasi-hydrostatic, and nonhydrostatic ocean modeling. *Journal of Geophysical Research: Oceans*, **102 (C3)**, 5733–5752.

Mazloff, M. R., P. Heimbach, and C. Wunsch, 2010: An eddy-permitting Southern Ocean state estimate. *Journal of Physical Oceanography*, **40 (5)**, 880–899.

McDougall, T. J., 1987: Neutral surfaces. *J. Phys. Oceanogr.*, **17 (11)**, 1950–1964.

Moholdt, G., L. Padman, and H. A. Fricker, 2014: Basal mass budget of Ross and Filchner-Ronne ice shelves, Antarctica, derived from Lagrangian analysis of ICESat altimetry. *Journal of Geophysical Research: Earth Surface*, **119 (11)**, 2361–2380.

Morrison, A. K., A. M. Hogg, M. H. England, and P. Spence, 2020: Warm Circumpolar Deep Water transport toward Antarctica driven by local dense water export in canyons. *Sci. Adv.*, **6 (18)**, eaav2516.

Mueller, R. D., T. Hattermann, S. L. Howard, and L. Padman, 2018: Tidal influences on a future evolution of the Filchner–Ronne Ice Shelf cavity in the Weddell Sea, Antarctica. *Cryosphere*, **12 (2)**, 453–476.

Muench, R. D., and A. L. Gordon, 1995: Circulation and transport of water along the western Weddell Sea margin. *J. Geophys. Res. Oceans*, **100 (C9)**, 18 503–18 515.

Naughten, K. A., A. Jenkins, P. R. Holland, R. I. Mugford, K. W. Nicholls, and D. R. Munday, 2019: Modeling the Influence of the Weddell Polynya on the Filchner–Ronne Ice Shelf Cavity. *J. Climate*, **32 (16)**, 5289–5303.

Naveira Garabato, A. C., E. L. McDonagh, D. P. Stevens, K. J. Heywood, and R. J. Sanders, 2002: On the export of Antarctic bottom water from the Weddell Sea. *Deep Sea Res. Pt. II*, **49 (21)**, 4715–4742.

Naveira Garabato, A. C., and Coauthors, 2017: Vigorous lateral export of the meltwater outflow from beneath an Antarctic ice shelf. *Nature*, **542 (7640)**, 219–222.

Newsom, E. R., C. M. Bitz, F. O. Bryan, R. Abernathey, and P. R. Gent, 2016: Southern Ocean deep circulation and heat uptake in a high-resolution climate model. *Journal of Climate*, **29 (7)**, 2597–2619.

Nicholls, K., L. Boehme, M. Biuw, and M. Fedak, 2008: Wintertime ocean conditions over the southern Weddell Sea continental shelf, Antarctica. *Geophysical Research Letters*, **35 (21)**.

Nicholls, K., S. Østerhus, K. Makinson, T. Gammelsrød, and E. Fahrbach, 2009: Ice-ocean processes over the continental shelf of the southern Weddell Sea, Antarctica: A review. *Reviews of Geophysics*, **47 (3)**.

Nicholls, K., S. Østerhus, K. Makinson, and M. Johnson, 2001: Oceanographic conditions south of Berkner Island, beneath Filchner-Ronne Ice Shelf, Antarctica. *Journal of Geophysical Research: Oceans*, **106 (C6)**, 11 481–11 492.

Nicholls, K. W., L. Padman, M. Schröder, R. A. Woodgate, A. Jenkins, and S. Østerhus, 2003: Water mass modification over the continental shelf north of Ronne Ice Shelf, Antarctica. *J. Geophys. Res. Oceans*, **108 (C8)**.

Nurser, A. J. G., and M.-M. Lee, 2004: Isopycnal averaging at constant height. Part II: Relating to the residual streamfunction in Eulerian space. *J. Phys. Oceanogr.*, **34 (12)**, 2740–2755.

Ohshima, K. I., and Coauthors, 2013: Antarctic Bottom Water production by intense sea-ice formation in the Cape Darnley polynya. *Nat. Geosci.*, **6 (3)**, 235–240.

Orsi, A. H., S. S. Jacobs, A. L. Gordon, and M. Visbeck, 2001: Cooling and ventilating the abyssal ocean. *Geophys. Res. Lett.*, **28 (15)**, 2923–2926.

Orsi, A. H., G. C. Johnson, and J. L. Bullister, 1999: Circulation, mixing, and production of Antarctic Bottom Water. *Progress in Oceanography*, **43 (1)**, 55–109.

Østerhus, S., 2006: Physical oceanography during ANDENES cruise NARE85. PANGAEA, URL https://doi.org/10.1594/PANGAEA.527497, doi:10.1594/PANGAEA.527497.

Padman, L., H. A. Fricker, R. Coleman, S. Howard, and L. Erofeeva, 2002: A new tide model for the Antarctic ice shelves and seas. *Annals of Glaciology*, **34 (1)**, 247–254.

Padman, L., S. L. Howard, A. H. Orsi, and R. D. Muench, 2009: Tides of the northwestern Ross Sea and their impact on dense outflows of Antarctic Bottom Water. *Deep Sea Res. Pt. II*, **56 (13-14)**, 818–834.

Plumb, R. A., and R. Ferrari, 2005: Transformed Eulerian-mean theory. Part I: Nonquasigeostrophic theory for eddies on a zonal-mean flow. *J. Phys. Oceanogr.*, **35 (2)**, 165–174.

Powers, J. G., K. W. Manning, D. H. Bromwich, J. J. Cassano, and A. M. Cayette, 2012: A decade of antarctic science support through amps. *Bulletin of the American Meteorological Society*, **93 (11)**, 1699–1712.

Robertson, R., 2001: Internal tides and baroclinicity in the southern Weddell Sea: 1. Model description. *J. Geophys. Res. Oceans*, **106 (C11)**, 27 001–27 016.

Schaffer, J., R. Timmermann, J. E. Arndt, D. Steinhage, and T. Kanzow, 2014: RTopo-2: A global dataset of ice sheet topography, cavity geometry and ocean bathymetry to study ice-ocean interaction in Northeast Greenland.

Schodlok, M. P., D. Menemenlis, and E. J. Rignot, 2016: Ice shelf basal melt rates around A ntarctica from simulations and observations. *J. Geophys. Res. Oceans*, **121 (2)**, 1085–1109.

Silvano, A., and Coauthors, 2020: Recent recovery of Antarctic Bottom Water formation in the Ross Sea driven by climate anomalies. *Nat. Geosci.*, 1–7.

Spence, P., S. M. Griffies, M. H. England, A. M. Hogg, O. A. Saenko, and N. C. Jourdain, 2014: Rapid subsurface warming and circulation changes of Antarctic coastal waters by poleward shifting winds. *Geophys. Res. Lett.*, **41 (13)**, 4601–4610.

Spence, P., R. M. Holmes, A. M. Hogg, S. M. Griffies, K. D. Stewart, and M. H. England, 2017: Localized rapid warming of West Antarctic subsurface waters by remote winds. *Nat. Clim. Change*, **7 (8)**, 595–603.

St-Laurent, P., J. M. Klinck, and M. S. Dinniman, 2013: On the role of coastal troughs in the circulation of warm Circumpolar Deep Water on Antarctic shelves. *Journal of Physical Oceanography*, **43 (1)**, 51–64.

Stanley, G. J., 2019: Neutral surface topology. *Ocean Modell.*, **138**, 88–106.

Stewart, A. L., 2019: Approximating Isoneutral Ocean Transport via the Temporal Residual Mean. *Fluids*, **4 (4)**, 179.

Stewart, A. L., and A. M. Hogg, 2017: Reshaping the Antarctic Circumpolar Current via Antarctic Bottom Water Export. *Journal of Physical Oceanography*, **47 (10)**, 2577–2601.

Stewart, A. L., A. Klocker, and D. Menemenlis, 2018: Circum-Antarctic shoreward heat transport derived from an eddy-and tide-resolving simulation. *Geophysical Research Letters*, **45 (2)**, 834–845.

Stewart, A. L., A. Klocker, and D. Menemenlis, 2019: Acceleration and overturning of the Antarctic Slope Current by winds, eddies, and tides. *J. Phys. Oceanogr.*, **49 (8)**, 2043–2074.

Stewart, A. L., and A. F. Thompson, 2013: Connecting Antarctic cross-slope exchange with Southern Ocean overturning. *Journal of Physical Oceanography*, **43 (7)**, 1453–1471.

Stewart, A. L., and A. F. Thompson, 2015a: Eddy-mediated transport of warm Circumpolar Deep Water across the Antarctic shelf break. *Geophysical Research Letters*, **42 (2)**, 432–440.

Stewart, A. L., and A. F. Thompson, 2015b: The neutral density temporal residual mean overturning circulation. *Ocean Modell.*, **90**, 44–56.

Stewart, A. L., and A. F. Thompson, 2016: Eddy generation and jet formation via dense water outflows across the Antarctic continental slope. *J. Phys. Oceanogr.*, **46 (12)**, 3729–3750.

Sun, S., I. Eisenman, L. Zanna, and A. L. Stewart, 2020: Surface Constraints on the Depth of the Atlantic Meridional Overturning Circulation: Southern Ocean versus North Atlantic. *J. Climate*, **33 (8)**, 3125–3149.

Talley, L. D., 2013: Closure of the global overturning circulation through the Indian, Pacific, and Southern Oceans: Schematics and transports. *Oceanogr.*, **26 (1)**, 80–97.

Thompson, A. F., and K. J. Heywood, 2008: Frontal structure and transport in the northwestern Weddell Sea. *Deep Sea Res. Pt. I*, **55 (10)**, 1229–1251.

Thompson, A. F., K. J. Heywood, S. Schmidtko, and A. L. Stewart, 2014: Eddy transport as a key component of the Antarctic overturning circulation. *Nat. Geosci.*, **7 (12)**, 879–884.

Thompson, A. F., A. L. Stewart, P. Spence, and K. J. Heywood, 2018: The Antarctic Slope Current in a Changing Climate. *Reviews of Geophysics*, **56 (4)**, 741–770.

Towns, J., and Coauthors, 2014: XSEDE: Accelerating scientific discovery. *Computing in Science Engineering*, **16 (5)**, 62–74, doi: 10.1109/MCSE.2014.80.

Vallis, G. K., 2017: *Atmospheric and oceanic fluid dynamics*. Cambridge University Press.

Vernet, M., and Coauthors, 2019: The weddell gyre, southern ocean: present knowledge and future challenges. *Rev. Geophys.*, **57**, 623–708.

Wåhlin, A. K., and Coauthors, 2020: Ice front blocking of ocean heat transport to an Antarctic ice shelf. *Nature*, **578 (7796)**, 568–571.

Walin, G., 1982: On the relation between sea-surface heat flow and thermal circulation in the ocean. *Tellus*, **34 (2)**, 187–195.

Wang, Q., S. Danilov, E. Fahrbach, J. Schröter, and T. Jung, 2012: On the impact of wind forcing on the seasonal variability of Weddell Sea Bottom Water transport. *Geophys. Res. Lett.*, **39 (6)**.

Wang, Q., S. Danilov, H. Hellmer, D. Sidorenko, J. Schroeter, and T. Jung, 2013: Enhanced cross-shelf exchange by tides in the western Ross Sea. *Geophys. Res. Lett.*, **40 (21)**, 5735–5739.

Wang, Q., S. Danilov, and J. Schröter, 2009: Bottom water formation in the southern Weddell Sea and the influence of submarine ridges: Idealized numerical simulations. *Ocean Modell.*, **28 (1-3)**, 50–59.

Winton, M., R. Hallberg, and A. Gnanadesikan, 1998: Simulation of density-driven frictional downslope flow in z-coordinate ocean models. *J. Phys. Oceanogrl.*, **28 (11)**, 2163–2174.

Wolfe, C. L., 2014: Approximations to the ocean's residual circulation in arbitrary tracer coordinates. *Ocean Modell.*, **75**, 20–35.

Wolfe, C. L., and P. Cessi, 2009: Overturning circulation in an eddy-resolving model: The effect of the pole-to-pole temperature gradient. *Journal of physical oceanography*, **39 (1)**, 125–142.

Yankovsky, E., and S. Legg, 2019: Symmetric and Baroclinic Instability in Dense Shelf Overflows. *J. Phys. Oceanogr.*, **49 (1)**, 39–61.

Zhang, J., and W. D. Hibler III, 1997: On an efficient numerical method for modeling sea ice dynamics. *Journal of Geophysical Research: Oceans*, **102 (C4)**, 8691–8702.

Zika, J. D., M. H. England, and W. P. Sijp, 2012: The ocean circulation in thermohaline coordinates. *J. Phys. Oceanogr.*, **42 (5)**, 708–724.